



# Enhanced alpha-amylase inhibition activity of amine-terminated PAMAM dendrimer stabilized pure copper-doped magnesium oxide nanoparticles

Jaison Jeevanandam<sup>a</sup>, Mara Gonçalves<sup>a</sup>, Rita Castro<sup>a</sup>, Juan Gallo<sup>b</sup>, Manuel Bañobre-López<sup>b</sup>, João Rodrigues<sup>a,c,\*</sup>

<sup>a</sup> CQM-Centro de Química da Madeira, Universidade da Madeira, Campus da Penteada, 9020-105 Funchal, Portugal

<sup>b</sup> Advanced (magnetic) theranostic nanostructures lab (AmTheNa), Nanomedicine group, International Iberian Nanotechnology Laboratory (INL), Braga 4715-330, Portugal

<sup>c</sup> School of Materials Science and Engineering, Center for Nano Energy Materials, Northwestern Polytechnical University, Xi'an 710072, China

## ARTICLE INFO

### Keywords:

MgO nanoparticles  
Dendrimers  
Dopants  
Antidiabetic activity  
Alpha-amylase enzyme

## ABSTRACT

The present work aims to prepare copper-doped MgO nanoparticles via a sol-gel approach and study their antidiabetic alpha-amylase inhibition activity with undoped MgO nanoparticles. The ability of G5 amine-terminated polyamidoamine (PAMAM) dendrimer for the controlled release of copper-doped MgO nanoparticles to exhibit alpha-amylase inhibition activity was also evaluated. The synthesis of MgO nanoparticles via sol-gel approach and optimization of calcination temperature and time has led to the formation of nanoparticles with different shapes (spherical, hexagonal, and rod-shaped) and a polydispersity in size ranging from 10 to 100 nm with periclase crystalline phase. The presence of copper ions in the MgO nanoparticles has altered their crystallite size, eventually modifying their size, morphology, and surface charge. The efficiency of dendrimer to stabilize spherical copper-doped MgO nanoparticles (ca. 30 %) is higher than in other samples, which was confirmed by UV-Visible, DLS, FTIR, and TEM analysis. The amylase inhibition assay emphasized that the dendrimer nanoparticles stabilization has led to the prolonged enzyme inhibition ability of MgO and copper-doped MgO nanoparticles for up to 24 h.

## 1. Introduction

In the 21st century, diabetes is one of the life-threatening illnesses among humans, next to cancer [1]. According to International Diabetes Federation (IDF), in 2021, about 537 million people between the ages of 20 and 79 are living with diabetes worldwide [2]. Further, IDF also reported that about one in ten people globally were affected by diabetes and its associated complications. The prediction is that in 2030 about 643 million people will have diabetes, and by the year 2045, around 783 million [3]. Hence, treatment modalities for curing diabetes have gained significant attention among researchers. Type 1 and 2 are the two common diabetes forms caused by either the inability of the pancreas to secrete insulin or the inability of the pancreatic cells to make use of the secreted insulin due to insulin resistance, respectively [4]. In both types, the inhibition of enzymes, such as alpha-amylase and alpha-glucosidase,

delays the carbohydrate breakdown in saliva, small intestine and limits postprandial glucose excursion in the blood [5]. Plant-based compounds are generally used as enzyme inhibitors to delay and reduce postprandial blood glucose excursion [6–8]. Even though these phyto-compounds are beneficial for diabetes treatment, the lack of stability and tedious formulation are the major limitations of these enzyme inhibitors [9,10]. In addition, uncontrolled inhibition of digestive enzymes, especially alpha-amylase, can lead to undigested starch in the large bowel, eventually leading to colonic fermentation, flatulence, gastrointestinal upset, and abdomen distension [11]. Thus, there is a huge demand for a novel drug that can selectively inhibit digestive enzymes without leading to any side effects in the diabetic patients.

Nowadays, nanoparticles are gathering researcher's attention to develop new diagnosis and treatment systems for diabetes [12]. Among these nanoparticles, metal oxide nanoparticles, such as iron oxide,

**Abbreviations:** IDF, International Diabetes Federation; PAMAM, Poly(amidoamine); Cu-MgO, Copper-doped Magnesium oxide; PDI, Polydispersity index; TG-DTA, Thermogravimetry-differential thermal analysis; SEM, Scanning electron microscope; TEM, Transmission electron microscope; DLS, Dynamic light scattering; XRD, X-ray diffraction; COD, Crystal open database; FTIR, Fourier transform infrared spectroscopy.

\* Corresponding author at: CQM-Centro de Química da Madeira, Universidade da Madeira, Campus da Penteada, 9020-105 Funchal, Portugal.

E-mail addresses: [joaoc@staff.uma.pt](mailto:joaoc@staff.uma.pt), [joaor@uma.pt](mailto:joaor@uma.pt) (J. Rodrigues).

<https://doi.org/10.1016/j.bioadv.2023.213535>

Received 2 January 2023; Received in revised form 16 June 2023; Accepted 19 June 2023

Available online 21 June 2023

2772-9508/© 2023 The Authors. Published by Elsevier B.V. This is an open access article under the CC BY license (<http://creativecommons.org/licenses/by/4.0/>).

copper oxide, lead oxide, magnesium oxide, zinc oxide, and manganese dioxide, either as prepared or functionalized, are under massive research as inhibitors of alpha-amylase and alpha-glucosidase enzyme, respectively [13–19]. It can be noted that compared to other metal oxide nanoparticles, magnesium oxide (MgO) nanoparticles possess enhanced enzyme inhibition ability via reactive oxygen species (ROS) release. This mechanism leads to high thermal and pressure stability, high conductivity, less toxicity toward normal cells, high bioactivity, biocompatibility, and bioavailability [20–22]. Hence, MgO nanoparticles, synthesized either via a physical, chemical, or biological approach, can be used as a potential enzyme inhibitor [23–25]. However, physical synthesis (e.g.: laser ablation) of MgO nanoparticles can lead to stable nanoparticles yet require a high energy source [26], whereas biological synthesis via bacterial, fungal, or plant extract can yield nanoparticles with low toxicity yet low stability [27]. Notably, chemical routes, especially via the sol-gel approach, can yield relatively less toxic MgO nanoparticles with high stability [28]. In addition, the sol-gel approach is simple, cost-effective, requires low reaction temperature, and yields a highly pure final product with a high surface-to-volume ratio and compositional control of the metal oxides [29,30]. However, agglomeration and polydispersity are the major issues in sol-gel synthesized nanoparticles. This issue can be overcome by incorporating metal dopants into the crystal structure, thus obtaining stable monodispersed nanoparticles [31]. Further, adding metal dopants has been proven to alter the crystal structure, eventually enhancing their physicochemical and even biological properties [32].

Even though doped nanoparticles possess enhanced biological properties than the nanoparticle itself, they must be reformulated to be applied for biological applications due to challenges related to bioavailability and targeted delivery [33,34]. Several studies indicated that distinct generations of dendrimers are highly beneficial in the formulation of various nanoparticles for desired biological applications [35–38]. Hence, dendrimers have been identified to be a potential formulation material to contrive metallic nanoparticles or nanomedicines for specific biomedical applications [39,40]. Thus, the present work aims to synthesize metal-doped MgO nanoparticles via a sol-gel approach and compare their antidiabetic alpha-amylase inhibition activity with undoped MgO nanoparticles. Copper was selected in this study as a potential dopant to reduce the defect in the MgO crystal via partial substitution due to its ionic radius (0.073 nm), which is similar to magnesium (0.072 nm) [41–45]. In addition, the ability of amine-terminated polyamidoamine (PAMAM) dendrimer to control the release of copper-doped MgO nanoparticles was, to our knowledge, also investigated for the first time.

## 2. Experimental procedure

### 2.1. Materials

Magnesium acetate tetrahydrate (molecular mass = 214.46 g/mol; purity = 99.5 %) as magnesium precursor was procured from Merck® (Portugal), whereas citric acid (molecular mass = 192.13 g/mol; purity = 99.5 %) as gelling agent was purchased from Chem-Lab (Belgium). Further, ethanol (molecular mass = 46.06 g/mol; purity = 96 %) as solvent, copper acetate monohydrate (molecular mass = 199.65 g/mol; purity = 100 %) and copper nitrate 2.5-hydrate (molecular mass = 232.59 g/mol; purity = 99 %) as dopant source was obtained from Riedel-de Haën (Germany). Amine-terminated fifth-generation PAMAM (G5-NH<sub>2</sub>-PAMAM) dendrimer suspended in an aqueous medium was obtained from Dendritech® (USA). All the chemicals required for the amylase inhibition assay were obtained from Merck® (Portugal) and Sigma-Aldrich® (Germany).

### 2.2. Sol-gel synthesis of MgO and Cu-doped MgO nanoparticles

The synthesis procedure of MgO nanoparticles was adopted from our

previous work with certain modifications [46]. An equimolar ratio (final concentration: 1 M) of magnesium precursor [magnesium acetate tetrahydrate; Mg(CH<sub>3</sub>COO)<sub>2</sub>·4H<sub>2</sub>O] and gelling agent [citric acid; C<sub>6</sub>H<sub>8</sub>O<sub>7</sub>] were dissolved separately in the solvent [ethanol; C<sub>2</sub>H<sub>5</sub>OH]. After dissolution, the citric acid solution was mixed with magnesium acetate to alter its pH from ~7 to 5 and initiate gel formation. The mixture was undisturbed for 3 h for the completion of gel formation, which was later aged for 16 h at room temperature (25 °C) and dried in a hot air oven (Mettler UM 100 oven) at 100 °C for 24 h. The resultant sample was termed as precalcinated magnesium oxide (MgO) powder. Similar procedures were followed for the synthesis of copper-doped magnesium oxide (Cu-doped MgO), where 1, 2, and 3 % (w/w) of dopant source [copper acetate monohydrate; Cu(CH<sub>3</sub>COO)<sub>2</sub>/copper nitrate 2.5-hydrate; Cu<sub>2</sub>H<sub>10</sub>N<sub>4</sub>O<sub>17</sub>] was mixed in solvent (ethanol) along with magnesium precursor. The resultant doped samples were termed copper-doped magnesium oxide powders. Later, thermogravimetric-differential thermal analysis (TG-DTA) was utilized to select calcination temperature to form MgO/Cu-doped MgO nanoparticles. Hence, the precalcinated powder samples were calcinated at 550, 650, and 750 °C for 2, 3, and 4 h to optimize the calcination procedure using Nabertherm® muffle furnace-L model at a heating rate of 5 °C/min for the formation of MgO and Cu-doped MgO nanoparticles as shown in Fig. 1.

### 2.3. Characterization of nanoparticle samples

Initially, Thermogravimetry/Differential Thermal Analysis (TG-DTA) technique using a NETZSCH STA 409 PC/PG equipment was utilized to identify the temperature and time of the calcination process. Further, the Dynamic Light Scattering (DLS) and Electrophoretic Light Scattering (ELS) technique (Malvern® Instruments, Zetasizer Nano ZS EN3600, Worcestershire, UK, equipped with a standard 633 nm laser) was used to analyze the samples (100 mg in 10 ml of ultrapure water of pH 6.5–7) for optimizing calcination temperature and time for the formation of MgO and copper-doped MgO nanoparticles. The samples' average particle size, polydispersity index (PDI), and zeta potential were identified for calcination optimization (100 mg of samples in 10 ml of ultrapure water of pH 6.5–7). The physicochemical characteristics of the nanoparticles, such as crystallinity, optical property, functional group, and morphology, were identified via X-Ray Diffractometer (XRD – Bruker® D8 Advance), Ultraviolet-visible (UV-Vis; PerkinElmer® Lambda 35) spectroscopy, Fourier Transform Infrared (FTIR; PerkinElmer® Spectrum Two) spectroscopy, Scanning Electron Microscopy, with Electron Dispersion Spectroscopy (SEM, EDS; Bench SEM Phenom ProX) and Transmission Electron Microscopy (TEM; JEOL JEM 2100 80–100 kV), respectively.

### 2.4. Stabilization of nanoparticles with amine-terminated PAMAM dendrimers

The stabilization procedure for the controlled release of nanoparticles, followed by Shi et al. (2006) was used in the present work with certain modifications [47]. In this study, MgO/Cu-doped MgO nanoparticles were dispersed in ultrapure water, where the G5-NH<sub>2</sub>-PAMAM dendrimer was added (0.5:0.1 ratio mg/ml;  $2.4 \times 10^{-4}$  M) under constant stirring at room temperature (25 °C) for 2 h (optimization of stabilization reaction time and volume of dendrimer was briefly explained in supplementary information section S.7.). The resultant stabilized nanoparticles were characterized using UV-Vis spectroscopy, FTIR, and DLS/ELS analysis. The stabilization efficiency was known by analyzing the absorbance at 292 nm (UV-Vis spectroscopy) of MgO/Cu-doped nanoparticles present in the supernatant and the stabilized samples due to the presence of oxygen [48]. Later, the final product was isolated via the decantation process, where the supernatant is removed. The precipitate was sonicated for 5 min and lyophilized using a Labconco Freeze Zone 4.5-l freeze drier system for further morphology analysis. SEM analysis was used to analyze the morphology of the optimized

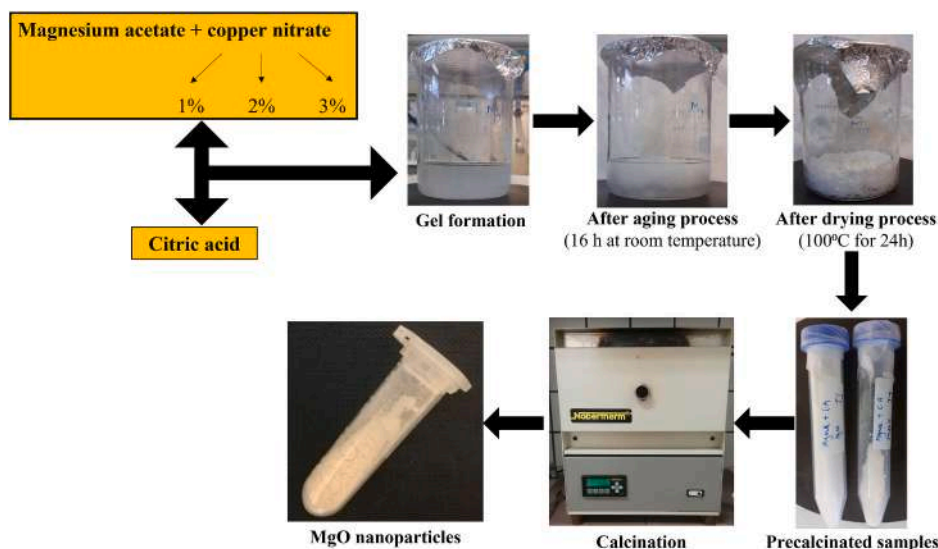


Fig. 1. Sol-gel synthesis approach for MgO nanoparticles and Cu-doped MgO nanoparticle formation.

dendrimer stabilized nanoparticle samples.

### 2.5. Alpha-amylase inhibition assay

The amylase inhibition activity as described by Ammulu et al. [15] was adopted in the current study with certain modifications. In the present work, the lyophilized alpha-amylase enzyme from human saliva (purchased from Sigma Aldrich®) was applied to identify the alpha-amylase inhibition activity of MgO, Cu-doped MgO, and dendrimer stabilized nanoparticle samples. Initially, the standard maltose graph shown in Fig. 2 was obtained using soluble maltose (2 mg/ml in ultra-pure water). After, 1–5 mg of MgO nanoparticles (spherical) were added to the mixture of starch, sodium chloride, and enzyme to identify the required concentration of nanoparticles for enzyme inhibition. The optical density (OD) value at 520 nm was substituted in the standard maltose graph to determine the concentration of maltose (starch converted into maltose due to enzyme) present in the test samples.

The formula

$$\text{Control} - \text{sample/control} \times 100$$

allowed the calculation of the percentage of enzyme inhibition by the

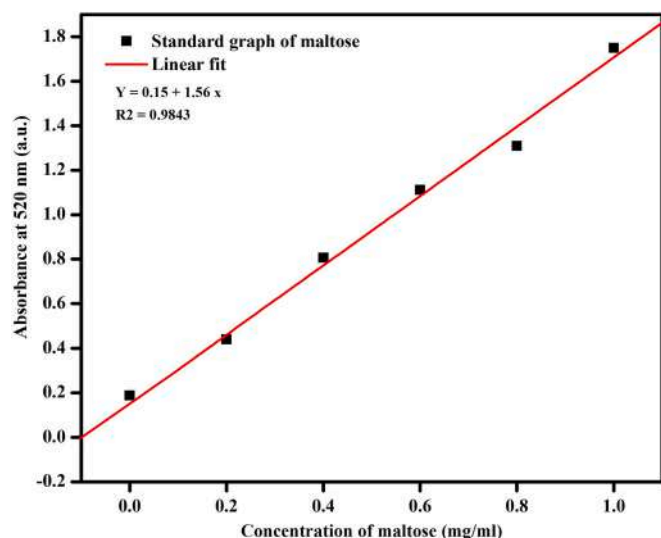


Fig. 2. Standard maltose calibration graph for amylase inhibition activity.

free and dendrimer stabilized nanoparticle samples after 0 and 24 h [15].

### 3. Results and discussion

It can be noted that the time for gel formation differs between samples due to the addition of different copper dopant sources. Rigid gel formation was observed in undoped samples, whereas the addition of dopants led to fluffy gel formation. The distinct gel formation is an indicator of dopants altering the physical and crystal structure of the precalcinated samples, which was evident from the DLS/ELS and yield analysis as shown in Fig. 3.

While comparing size and PDI (supplementary information, section S.1.), the results as displayed in Fig. 3 (A) denotes that the copper dopant via copper acetate increases the size of the particle and leads to polydispersity and agglomeration, which can be avoided during the calcination process. Further, the hydrodynamic particle size of the samples with copper nitrate as a dopant source is lower compared to copper acetate samples. Furthermore, it can be noted that the copper dopant has increased the particle size, compared to non-doped samples. This shows that the inorganic dopant source (ionic bonds) will lead to lower hydrodynamic particle size, compared to organic precursor (covalent bonds), due to their solubility difference [49]. Although the error bars of the samples are higher due to polydispersity (rapid agglomeration), the PDI of precalcinated MgO is 0.4 (monodispersity with certain agglomeration). In contrast, the PDI of precalcinated Cu-doped MgO sample with copper acetate and copper nitrate as dopant sources is above 0.5 (polydisperse) because of the addition of copper. Further, the error percentage associated with the zeta potential value is also high due to rapid agglomeration [50]. Notably, the addition of a distinct percentage of copper has led to the alteration of precalcinated Cu-doped MgO sample's zeta potential from negative to zero (neutral stability) as indicated in Fig. 3 (B). This denotes that the negative charges due to oxygen presence in precalcinated MgO sample are replaced by the copper ions (positive surface charge) [51,52]. However, the error of the zeta value is also high due to rapid agglomeration, but only for 3 % Cu-doped sample. While using copper nitrate as a dopant source, the surface charge of precalcinated MgO and Cu-doped MgO is below zero (−2.5 to 0 mV range), which indicates that the copper is not doped on the surface. The copper may have replaced the magnesium ions in the crystal via partial substitution, which eventually led to the negative charge of precalcinated MgO sample due to oxygen [45]. This denotes that the negative charge is due to oxygen presence in precalcinated MgO sample,

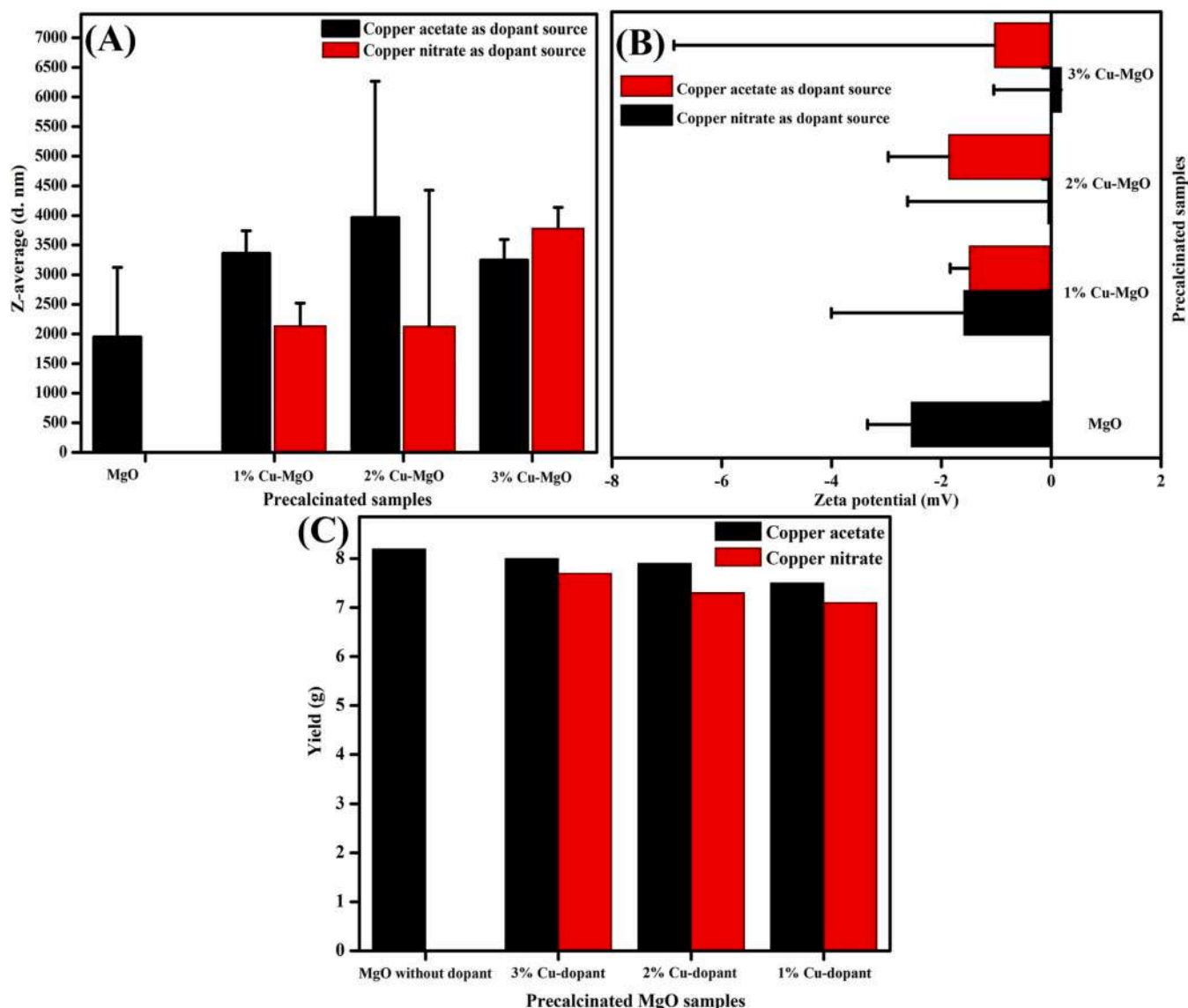


**Fig. 3.** Characterization of precalculated Cu-doped MgO samples with copper acetate and copper nitrate as dopant sources (A) Average particle hydrodynamic diameter by DLS; (B) Average zeta potential by ELS; and (C) mass yield.

where more Mg ions (smaller ionic radii) are replaced with copper ions (larger ionic radii leading to slightly higher positive surface charge) during the doping process. This process can be attributed to the increase in copper content (due to dopant percentage increase), where the copper ions at the nanoparticle surface may be sub-coordinated to oxide ions and leads to fluctuations in their zeta potential [51,52]. Fig. 3 (C) shows the precalculated samples' yield, indicating that the doping process has reduced the reaction yield. This reduction can be due to the oxygen replacement in the precalculated MgO crystal by copper (copper acetate) or replacing magnesium in the crystal (copper nitrate). In the case of copper acetate, the replacement of a few oxygen atoms via a different percentage of copper (denoted by an increase in zeta potential) may have contributed to the yield reduction. Even though oxygen (atomic mass = 15.9 u) is replaced by copper (atomic mass = 63.5 u), the remaining oxygen forms precalculated MgO like a chain in the gel. In the case of copper nitrate, the magnesium (atomic mass = 24.3 u) ion is replaced by copper, which would have led to the release of magnesium from the crystal core (disrupts crystal form) and are eliminated during the drying process (100 °C for 24 h) along with ethanol as a byproduct. There may be a chance for copper to be present in place of magnesium between gel bonds via partial substitution, which may have reduced the

formation of a few precalculated MgO crystals during gel formation [45,53,54]. Thus, copper nitrate was selected as a dopant source for further analysis as size (size variation gradually increases), PDI (poly-dispersed), and zeta potential (negative charge) are promising compared to copper acetate, even though the yield is slightly lower.

### 3.1. Thermogravimetry analysis

Fig. 4 (A-D) shows the TG-DTA analysis of precalculated MgO and Cu-doped MgO samples with three degradation stages. The results showed that the crystalline water and carbon dioxide are released in the first thermal degradation stage from ~30–200 °C, whereas the precalculated MgO sample is transformed to MgO nanoparticles in the second thermal degradation stage at ~200–480 °C. It can be noted that between the temperatures ~480–800 °C, there are certain weight losses in the sample, which shows that the calcination at these temperatures can lead to shape modification (comparison table included in supplementary information S.2.9.) [28,55,56]. Above 800 °C, the resultant MgO will be at a stable crystalline state with high thermal stability. Hence, its crystal structure cannot be modified above this temperature. Further, DTA shows that the weight loss and thermal degradation is due



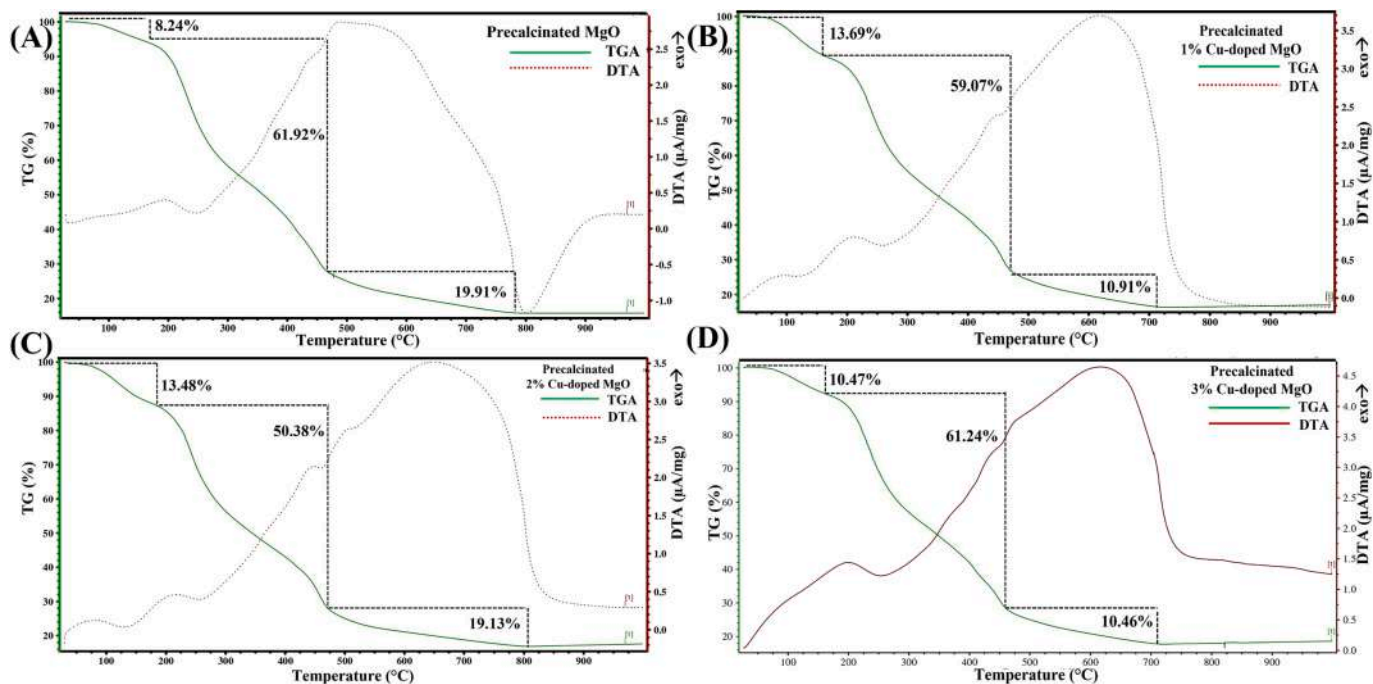


Fig. 4. TG-DTA analysis of precalcinated (A) MgO; (B) 1 % Cu-doped MgO; (C) 2 % Cu-doped MgO and (D) 3 % Cu-doped MgO samples.

to the exothermal reaction, which corresponds to the weight loss. During the third degradation, DTA decreases, indicating that MgO nanoparticles are formed due to weight loss via endothermic reaction. In addition, the difference in weight loss percentage can be attributed to the addition of distinct copper dopant percentages and copper ions in the crystal structure of precalcinated samples [57–59]. Thus, the temperature above 480 °C (2nd degradation) is selected, especially 80–100 °C above second thermal degradation temperature as calcination temperature to alter the shape of nanoparticles [60,61]. The formation of MgO nanoparticles above glass transition temperature has been proven by XRD analysis in Section 3.3. Hence, three distinct temperatures, such as 550, 650, and 750 °C for 2, 3, and 4 h were selected to calcinate the samples for forming nanoparticles with different morphologies.

### 3.2. DLS/ELS analysis of calcinated samples

Table 1 shows the DLS analysis results (data in supplementary information; section S.2.), which shows the average particle size, PDI, and zeta potential of the calcinated and Cu-doped MgO samples. It is worth noting from the table that the MgO nanoparticles are formed, where the temperature and reaction time plays a significant role in their size, morphology, dispersity, and surface charge [28,62]. Calcinated samples with smaller size, high stability, and PDI below 0.5 were fixed as the criteria for sample selection that can be subjected to further characterization. Accordingly, the selected samples that yielded spherical, hexagonal, and rod-shaped MgO nanoparticles were calcinated at 550 °C for 4 h, 650 °C for 2 h, and 750 °C for 3 h, respectively. Similarly, 1, 2, and 3 % Cu-doped samples calcinated at 550 °C for 2 h, 650 °C for 4 h, and 750 °C for 4 h, respectively, were also selected to yield spherical, hexagonal, and rod-shaped Cu-doped MgO nanoparticles. The comparison between the DLS/ELS data of calcinated MgO and Cu-MgO samples showed that the copper acting as a dopant has reduced the size, and PDI, which eventually increased the stability of the resultant MgO nanoparticles, compared to precalcinated samples [63]. However, the fluctuations in the particle size due to varying dopant concentration, calcination temperature, and time was erratic and further detailed thermodynamic studies must be performed in the future to confirm the influence of these parameters [64,65].

Table 1

DLS/ELS analysis of calcinated MgO and Cu-doped MgO (Cu-MgO) samples.

Calcinated Sample	Calcination temperature and time	Z-average (d. nm)	PDI	Zeta potential (mV)
MgO	550 °C, 2 h	342	0.73	−6.5
	550 °C, 3 h	396.1	0.74	−4.9
	550 °C, 4 h	91.28	0.72	−2.9
	650 °C, 2 h	78.82	0.43	−7
	650 °C, 3 h	91.28	0.35	11.2
	650 °C, 4 h	825	0.32	19.2
	750 °C, 2 h	91.28	0.75	−10.7
	750 °C, 3 h	68.06	0.39	20.5
	750 °C, 4 h	955.4	0.66	−1.4
1 % Cu-MgO	550 °C, 2 h	78.82	0.43	3.8
	550 °C, 3 h	58.77	0.46	18.7
	550 °C, 4 h	122.4	0.51	10
	650 °C, 2 h	531.2	0.51	−8.2
	650 °C, 3 h	122.4	0.72	21.1
	650 °C, 4 h	50.75	0.47	23.6
	750 °C, 2 h	68.06	0.48	−21.8
	750 °C, 3 h	78.82	0.49	17
	750 °C, 4 h	164.2	0.32	16
2 % Cu-MgO	550 °C, 2 h	342	1	−22.9
	550 °C, 3 h	122.4	0.76	18.4
	550 °C, 4 h	1106	0.57	−13.1
	650 °C, 2 h	825	0.90	−18.6
	650 °C, 3 h	58.77	0.65	21
	650 °C, 4 h	68.06	0.37	23.8
	750 °C, 2 h	91.28	0.72	16.3
	750 °C, 3 h	122.4	0.60	20.7
	750 °C, 4 h	91.28	0.37	23.8
3 % Cu-MgO	550 °C, 2 h	78.82	0.46	20.8
	550 °C, 3 h	78.82	0.55	20.3
	550 °C, 4 h	458.7	0.82	−21.4
	650 °C, 2 h	712.4	0.84	13.1
	650 °C, 3 h	68.06	0.31	18.8
	650 °C, 4 h	78.82	0.31	19.8
	750 °C, 2 h	91.28	0.53	22.9
	750 °C, 3 h	105.7	0.27	24.4
	750 °C, 4 h	78.82	0.23	19.6

### 3.3. Crystallinity analysis

The XRD analysis was utilized to identify the crystallinity of the precalcinated and calcinated MgO samples, as shown in Fig. 5. The XRD data of all the precalcinated samples (Fig. 5 (A) and (B)) showed that the

peaks are not present, which indicated that they are amorphous. However, it can be noted that the calcination process has led to the formation of pure crystalline MgO particles. The XRD analysis of the selected calcinated MgO nanoparticle at 550 °C for 4 h (Fig. 5 (C)) possesses characteristic peaks which are exactly matching with the periclase

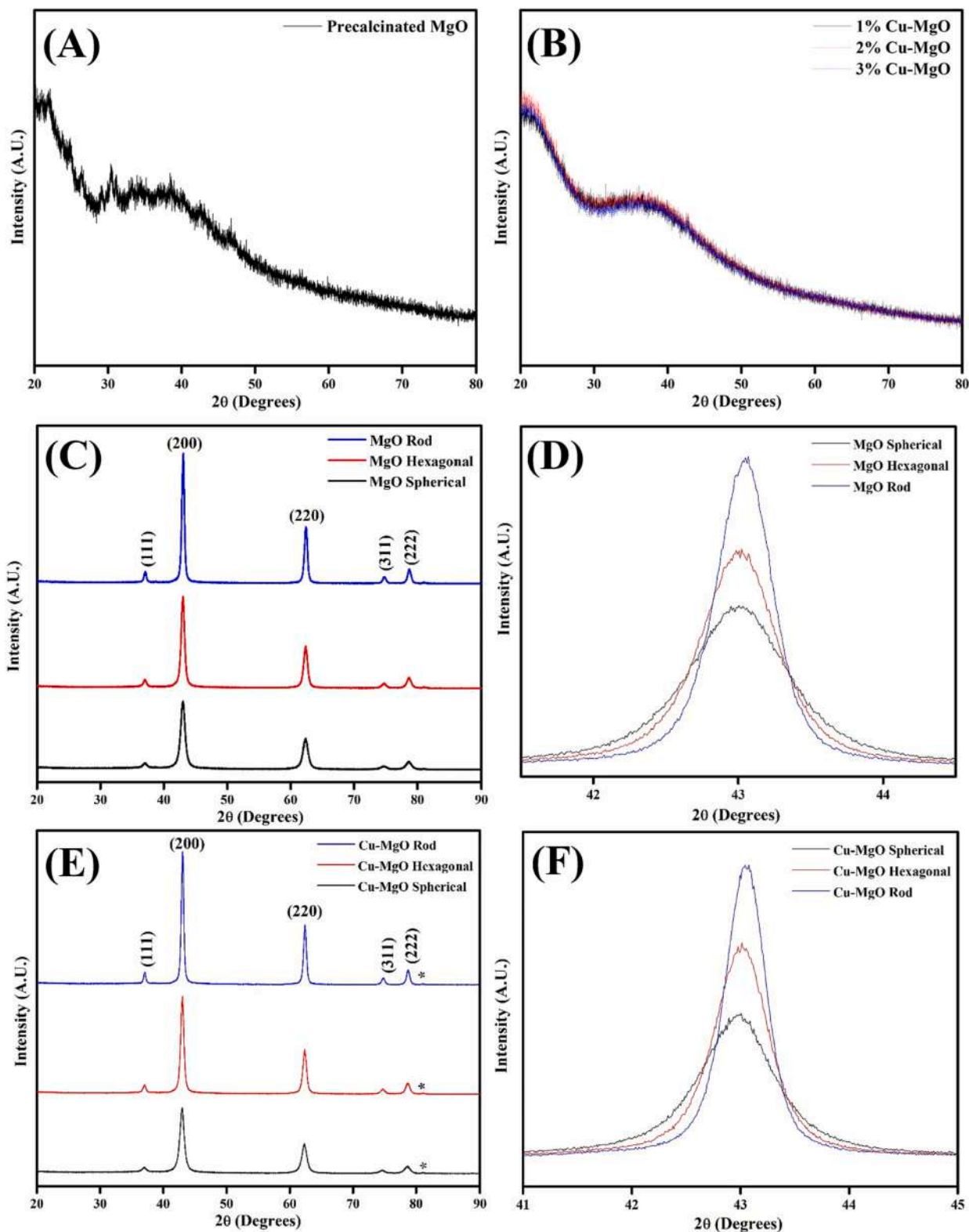


**Fig. 5.** XRD spectra of (A) precalcinated MgO, (B) precalcinated 1, 2, 3 % of Cu-doped MgO, and (C) calcinated MgO and Cu-doped MgO samples at different temperature leading to distinct (expected) morphology, (D) and (F) Full width of characteristic MgO crystal peak at  $2\theta = 42.9^\circ$ .

crystalline phase of MgO [COD – crystal open database 00–900-6790; Supplementary information section S.3] [66,67]. The full width half maximum (FWHM) of the samples has been identified (using the non-linear fit of peaks) as 0.9138 at 42.9° of 2 $\theta$ . Scherrer's formula has been used to identify the crystallite size of the sample.

$$\text{Scherrer's formula } D = 0.9\lambda/\beta\cos\theta$$

where, 0.9 = Scherrer constant;  $\lambda$  = wavelength of x-rays. In the present study, Bruker X8 XRD equipment was utilized, which uses Cu K $\alpha$  with a wavelength of 1.56 Å;  $\beta$  = FWHM and  $\theta$  is the corresponding angle of FWHM. An increase in the calcination temperature has led to an increment in the peaks of FWHM. This observation indicates that the calcination has improved the crystallinity and contributed to the shape alteration [68], as Fig. 5 (D) pointed out.

In Cu-doped calcinated samples, there is a minor peak after 80°, which is formed due to the addition of copper ions [69]. Further, it is noteworthy that the XRD peak of Cu-MgO samples (Fig. 5 (E) and (F)) are also similar to MgO (same crystal phase structure) with similar peaks of Cu<sub>2</sub>O (cuprous oxide) but with distinct peak intensity [JCPDS 05–0667] [70]. It is evident from the XRD results that there is a minute deflection in the peak position and intensity compared to MgO and COD file data of the reference MgO XRD peak. This confirms that the dopants are present in the sample after calcination and leads to the formation of pure MgO crystals with slight phase modifications [71,72].

The crystallite size calculation using Scherrer's formula showed that the crystals gradually grow concerning the calcination temperature, as listed in Table 2. The MgO sample calcinated at 550 °C possesses 9 ± 0.08 nm of crystallite size, whereas the addition of 1 % copper as a dopant has led to a similar crystallite size (9 ± 0.16 nm). In samples calcinated at 650 °C, the MgO sample possesses 12 ± 0.28 nm of crystallite size, whereas the 2 % copper doping increased their crystallite size (13 ± 0.08 nm). Further, the MgO sample possesses 17 ± 0.05 nm of crystallite size, whereas the 3 % copper doping increased their crystallite size (17 ± 0.23 nm) in samples calcinated at 750 °C. The similar or increased crystallite size in doped samples is due to the morphology transformation, which must have been initiated by the crystal structure change compared to undoped MgO samples [58,73]. The crystallite size of the MgO sample is 9 ± 0.08 nm, whereas the average particle size predicted via DLS analysis is 91.28 nm. As expected, the study emphasized that the crystallite size of all the samples is lower than the DLS values, which refers to the hydrodynamic size. The crystallites together form nanoparticles [74,75], and thus, the result shows that the size of the nanoparticles will be lesser or closer to DLS results due to the interaction of aqueous medium and spherical approximation in DLS analysis [76].

### 3.4. Functional group analysis

Fig. 6 shows the FTIR spectra of precalcinated and calcinated MgO as well as Cu-doped MgO samples. Table S.4 (A) and (B) in supplementary

material summarize FTIR spectral peaks for comparing the vibrational groups and their respective functional groups present in precalcinated and calcinated samples. The attenuated total reflectance (ATR) method was used to analyze precalcinated MgO samples, whereas the potassium bromide (KBr) method was used to analyze calcinated MgO samples. It is evident that the reflectance property of precalcinated samples is reduced due to the formation of nanosized MgO, where size reduction has led to a difference in their property [77,78]. In precalcinated MgO sample, the presence of O—H group is due to hydroxide [(OH)<sub>2</sub>] in the magnesium complex before calcination and C—O group is due to the atmospheric CO<sub>2</sub> absorption by the sample. When compared to calcinated MgO samples, the peak difference at 618 cm<sup>−1</sup> indicates the presence of hydroxide complex in the material [79,80]. Meanwhile, the presence of O—H and C—O group in MgO sample is due to the absorbance of water and CO<sub>2</sub> from the atmosphere. The characteristic peak at 563 cm<sup>−1</sup> indicates the presence of Mg—O in the sample [81,82]. Further, the O—H group in precalcinated Cu-doped MgO samples is due to the existence of hydroxide [(OH)<sub>2</sub>], while the presence of C—O group is due to the absorption of CO<sub>2</sub> from the atmosphere. The peak difference at ~616 cm<sup>−1</sup> indicates the influence of copper ions on the hydroxide complex in the precalcinated Cu-doped samples compared to calcinated doped samples [83]. The peak at ca. 850 cm<sup>−1</sup> represents the presence of magnesium, and the peak at ca. 620 cm<sup>−1</sup> is due to the presence of hydroxide (precalcinated sample), whereas the peaks at 570 and 420 cm<sup>−1</sup> represents the oxide in the calcinated sample [46,66]. It is evident that several carboxylic acid peaks which are present in the precalcinated samples are missing in calcinated samples due to the transformation of magnesium complex to MgO. The same trend is also identified in the doped samples. Similarly, a few additional minor peaks are present in doped samples, which is not present in pure MgO samples due to the addition of dopants [84,85]. In addition, the minor peaks can also be due to the oxidation process in the sample, which replaces certain functional groups and shift their position. It can also be noted that certain peaks are missing in undoped and doped samples, indicating the structural difference induced by the doping process in the sample as functional groups [63,86,87]. Thus, it is apparent that the synergistic effect of calcination temperature, time, and dopants can effectively alter the functional groups in the MgO samples, which is evident in the DLS/ELS analysis as variation in the zeta potential, PDI, and average size.

### 3.5. Morphology analysis of MgO samples

The morphology of the precalcinated samples was analyzed using SEM (without gold sputtering), and elemental analysis was performed using Electron Dispersion Spectroscopy (EDS), as displayed in Fig. 7. The SEM results showed that the precalcinated samples are above 1000 nm in size, which is matching with the DLS results [88]. The EDS results (Fig. 7) revealed the presence of elements such as carbon (probably due to adhesive carbon tape in the sample holder or in the sample), magnesium, and oxygen, in the undoped precalcinated sample. The presence of a reduced atomic percentage of magnesium and more oxygen indicates that the magnesium ion will be in the core of the crystal, where hydrogen and oxygen from the precursor (acetate) are in the edges or interstitial position of the crystal [89,90]. However, the EDS results in Fig. S.5 (A–C) showed that copper was not detected in the metal-doped samples, suggesting that precalcinated samples do not contain copper. The observed morphology changes in the doped samples indicate that the copper ions may have been doped inside the crystal of the precalcinated sample [91]. Further, the fluctuation in the percentage of magnesium and oxygen is due to the polydispersity nature of the precalcinated samples [92,93]. The SEM analysis of the calcinated MgO samples was presented in Supplementary information S.5. It is not possible to view the particles via SEM images as the size of the particles is reduced to nano-regime and also because the MgO, resulting from the conversion of precalcinated magnesium, is an insulator and cannot conduct electrons [94,95]. Thus, TEM analysis was used to identify the

**Table 2**  
Crystallite size of calcinated MgO and Cu-doped MgO samples with standard deviation (SD).

Sample name	Calcination temperature	Calcination time (h)	Doping (%)	Expected morphology	Crystallite size (nm) ± SD
MgO	550 °C	4	–	Spherical	9 ± 0.08
MgO	650 °C	2	–	Hexagonal	12 ± 0.28
MgO	750 °C	3	–	Rod	17 ± 0.05
Cu-MgO	550 °C	2	1	Spherical	9 ± 0.16
Cu-MgO	650 °C	4	2	Hexagonal	13 ± 0.08
Cu-MgO	750 °C	4	3	Rod	17 ± 0.23

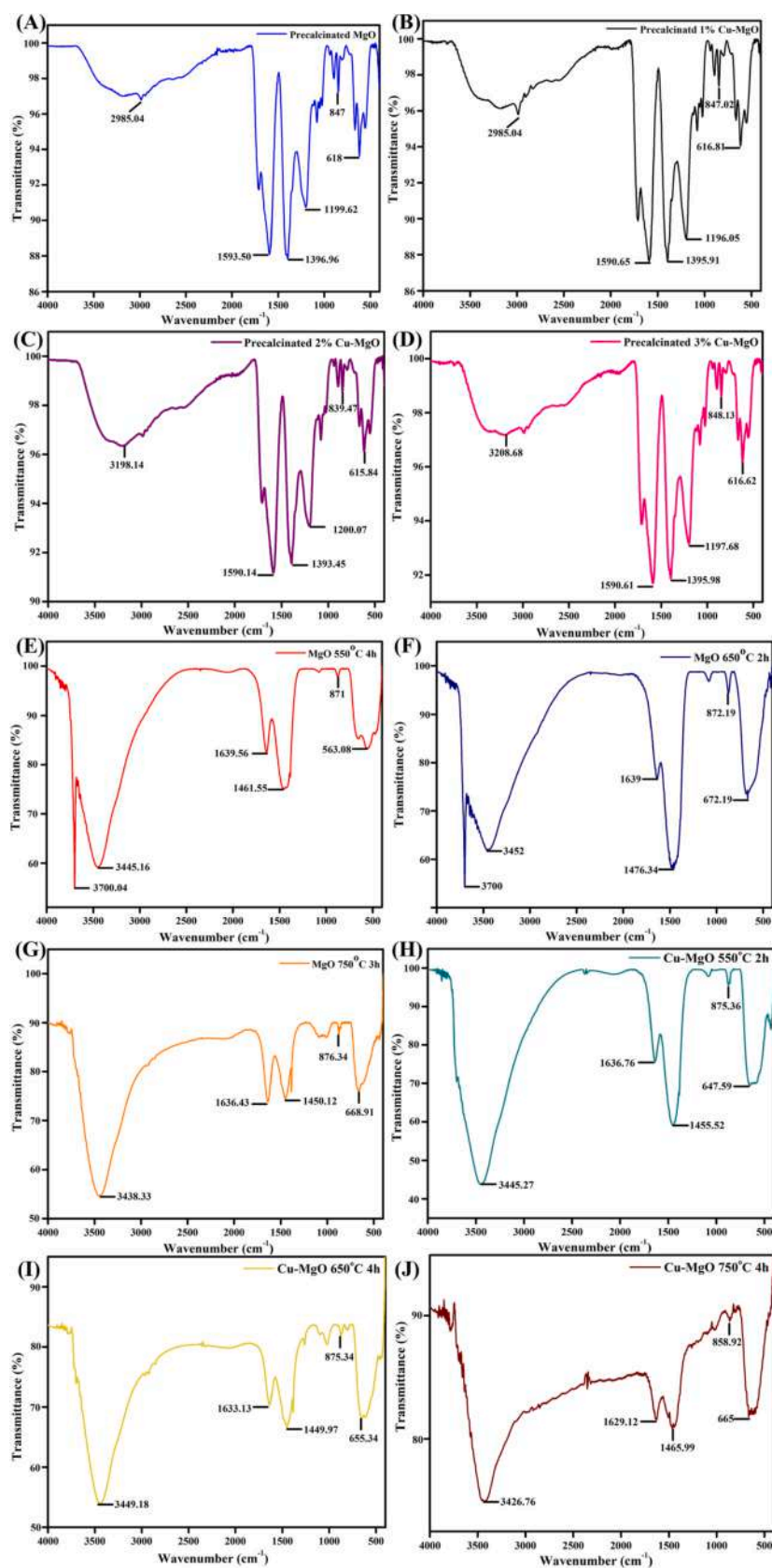


**Fig. 6.** FTIR spectra of precalcinated (A) MgO, (B) 1 % Cu-doped MgO, (C) 2 % Cu-doped MgO, (D) 3 % Cu-MgO, Calcined (E) MgO at 550 °C, (F) MgO at 650 °C, (G) MgO at 750 °C, (H) 1 % Cu-doped MgO at 550 °C, (I) 2 % Cu-doped MgO at 650 °C and (J) 3 % Cu-doped MgO at 750 °C.



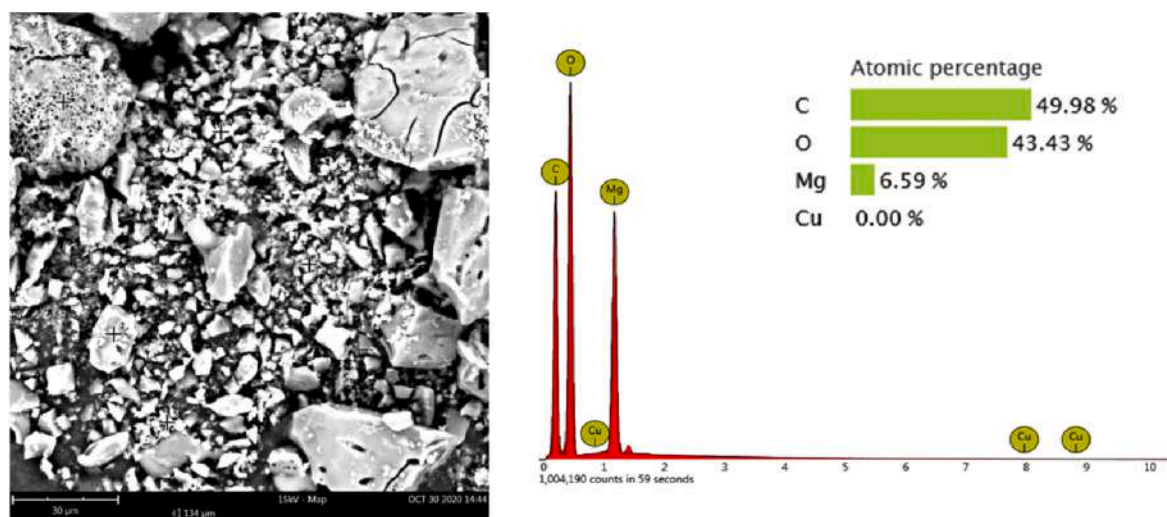


Fig. 7. Scanning electron micrograph and elemental analysis of precalcinated MgO sample (scale = 30  $\mu$ m).

morphology of the calcinated samples.

Fig. 8 (A–F) shows the TEM images of calcinated MgO and Cu-doped MgO nanoparticles. The size of the resultant nanoparticles was in the range of ca. 60–100 nm. The shape predicted via DLS and XRD analysis, such as spherical, hexagonal, and rod (elongated hexagon) calcinated at 550, 650, and 750  $^{\circ}$ C is almost similar in most of the samples as indicated by TEM images. Also, the agglomeration indicated by the DLS/ELS analysis also matches the images. The smaller-sized nanoparticles with predicted shapes (transformation from spherical to hexagon to elongated hexagon/rod) has been formed via the influence of calcination temperature, time, and dopant incorporation. However, the shape transformation in copper-doped samples were not evident, especially the rod shape, which may be due to insufficient calcination temperature or time [96]. Further, the solvent used to suspend the samples (ethanol) has led to agglomeration, similar to water. Thus, an alternative solvent or addition of surfactant is required to suspend MgO samples for TEM characterization to provide images without/less agglomeration [46].

### 3.6. Influence of calcination and dopants on MgO structure

Fig. 9 shows the possible mechanism of the sol-gel process in the formation of MgO and Cu-doped MgO nanoparticles and the influence of dopants and calcination on their morphology. The hydrolysis and condensation process has led to the formation of sol due to pH alteration from 7 (neutral) to 5 (acidic) when the gelling agent citric acid dissolved in ethanol was mixed with the magnesium and dopant precursors dissolved in ethanol [97]. Later, the sol is transformed into wet gel via the aging process, where the elements of precursors, gelling agent, and solvent arrange themselves as a matrix in the gel [98]. Further, the wet gel is allowed to evaporate via the drying process, where the excess ethanol is removed to form xerogel [99]. The xerogel was converted into nanoparticles of spherical, hexagonal, and rod (elongated hexagon) shape via the calcination process, which was confirmed by XRD and TEM analysis. It can be noted that the ionic radius of copper (0.073 nm) is similar to magnesium (0.072 nm), which allows the copper ions to replace magnesium ions of the magnesium complex via partial substitution during the hydrolysis and condensation process to reduce the defects in their amorphous structure [45,100]. The shape difference observed via SEM analysis, elemental analysis using EDS analysis, and crystallite sizes calculated via XRD analysis confirm these attributes, which is due to the replacement of magnesium ions with copper ions of amorphous precalcinated samples [45,101]. Later, the calcination led to the transformation of shapes from spherical to hexagon and hexagon to elongated hexagon and rod [102,103]. The use of FTIR, SEM, and TEM

analysis confirmed that doping with copper and calcination has led to modifications in the morphology of the copper-doped MgO nanoparticles compared to undoped MgO nanoparticles.

### 3.7. Stabilization efficiency of MgO nanoparticles using PAMAM dendrimers

The MgO nanoparticles synthesized via sol-gel approach are larger  $\sim$ 10–100 nm, compared to fifth-generation dendrimers, and thus, amine-terminated fifth-generation PAMAM dendrimer was used as a stabilizing agent for the controlled release of MgO nanoparticles. The standard calibration graph of MgO nanoparticles was obtained via UV-Visible spectroscopy by suspending 10 mg/ml of sample in ultrapure water as shown in supplementary information S.6. Figs. 10 (A) and (B) shows the absorbance of the dendrimer stabilized spherical MgO nanoparticle sample as well as supernatant (free dendrimer/MgO). The characteristic peak at 292 nm indicates the presence of a high concentration of MgO, which was eventually reduced in the supernatant (refer to supplementary information section S.7). In addition, the peak around 280 nm is present only in dendrimer stabilized spherical MgO sample, which may be due to the existence of free dendrimer along with nanoparticles stabilized with dendrimer refer to supplementary information section S.8.1). It is evident from Figs. 10 (C) and (D) that the dendrimer effectively stabilized the spherical and rod/elongated hexagon-shaped copper-doped MgO nanoparticles compared to undoped samples. However, the stabilization efficiency of hexagonal copper doped nanoparticles is less than undoped hexagonal nanoparticles. This observation can be attributed to the doped sample's edge atoms and the presence of copper ions in the MgO crystal's interstitial position, which may have restricted the crucial electrostatic attraction between the dendrimer and the nanoparticle [104–107], as schematically represented in Fig. 10 (E).

### 3.8. DLS/ELS analysis of PAMAM stabilized MgO nanoparticles samples

The average particle size predicted from DLS analysis showed that the stabilized samples are in the size range of  $\sim$ 700–900 nm, as indicated in Table 3. The wide range of particle size with PDI as 1 in supernatant samples indicates the presence of both dendrimer and nanoparticles that are not involved in the stabilization process. The increment in the size is due to the stabilization process. The zeta potential seems to decrease in the dendrimer stabilized samples. The alteration of zeta potential from negative to positive in spherical and hexagonal MgO nanoparticles samples is attributed to the terminal amine functionalization, whereas in rod-shaped MgO sample, the

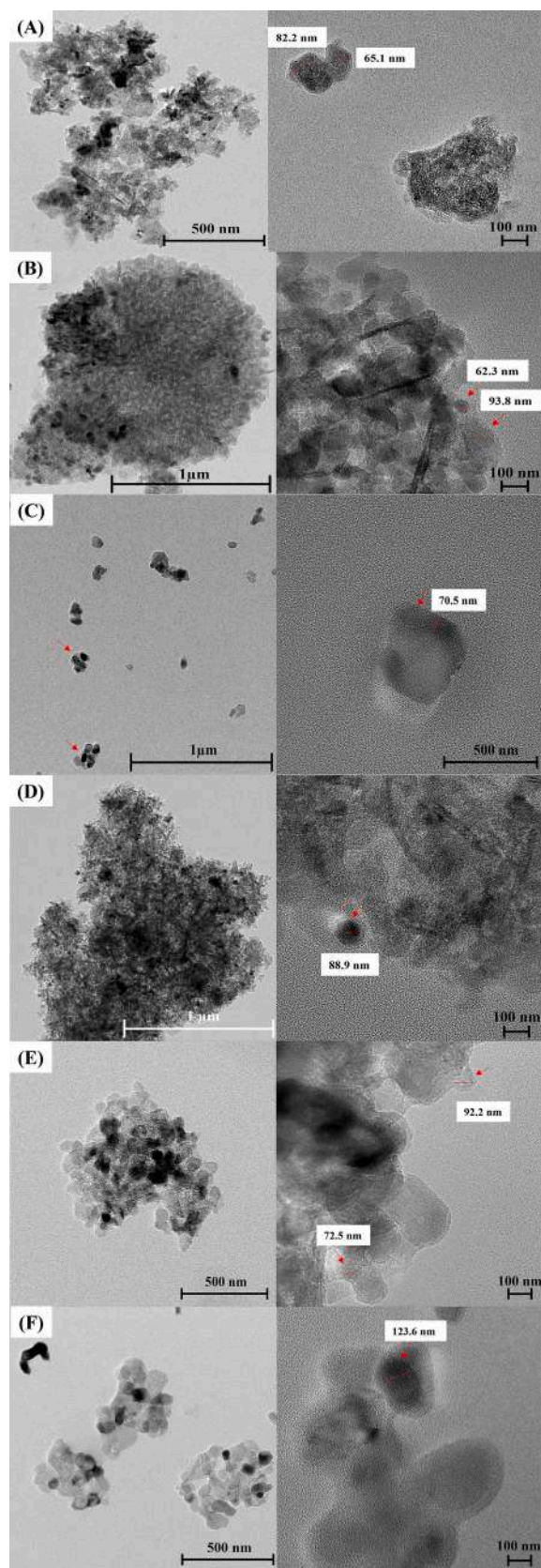


**Fig. 8.** TEM images in 1  $\mu\text{m}$ /500 nm/100 nm scale of calcinated MgO nanoparticles at (A) 550  $^{\circ}\text{C}$ , (B) 650  $^{\circ}\text{C}$ , (C) 750  $^{\circ}\text{C}$ ; (D) 1 % Cu-doped MgO nanoparticles calcinated at 550  $^{\circ}\text{C}$ , (E) 2 % Cu-doped MgO nanoparticles calcinated at 650  $^{\circ}\text{C}$  and (F) 3 % Cu-doped MgO nanoparticles calcinated at 750  $^{\circ}\text{C}$ .

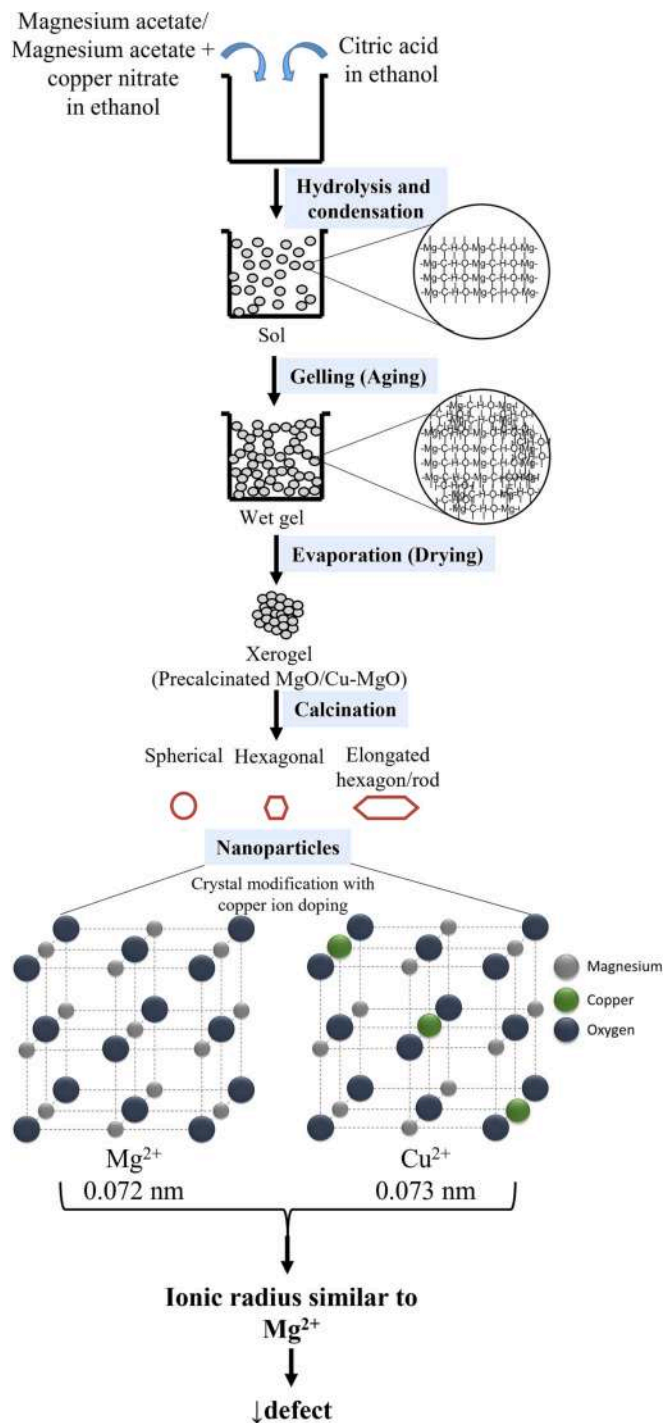


**Fig. 9.** Possible mechanism of MgO/Cu-doped MgO nanoparticle formation via sol-gel, doping, and calcination process.

positive charge decreases as the negatively charged oxygen group in the MgO nanoparticle is exposed to the surface during stabilization process [108,109]. A similar process (as in rod-shaped MgO) has also been observed in Cu-doped MgO nanoparticle samples. While comparing the data from UV-Visible spectra and DLS analysis, it is evident that the MgO nanoparticles were effectively stabilized by amine-terminated dendrimers (Additional data on optimization of stabilization is presented in supplementary information section S.8.).



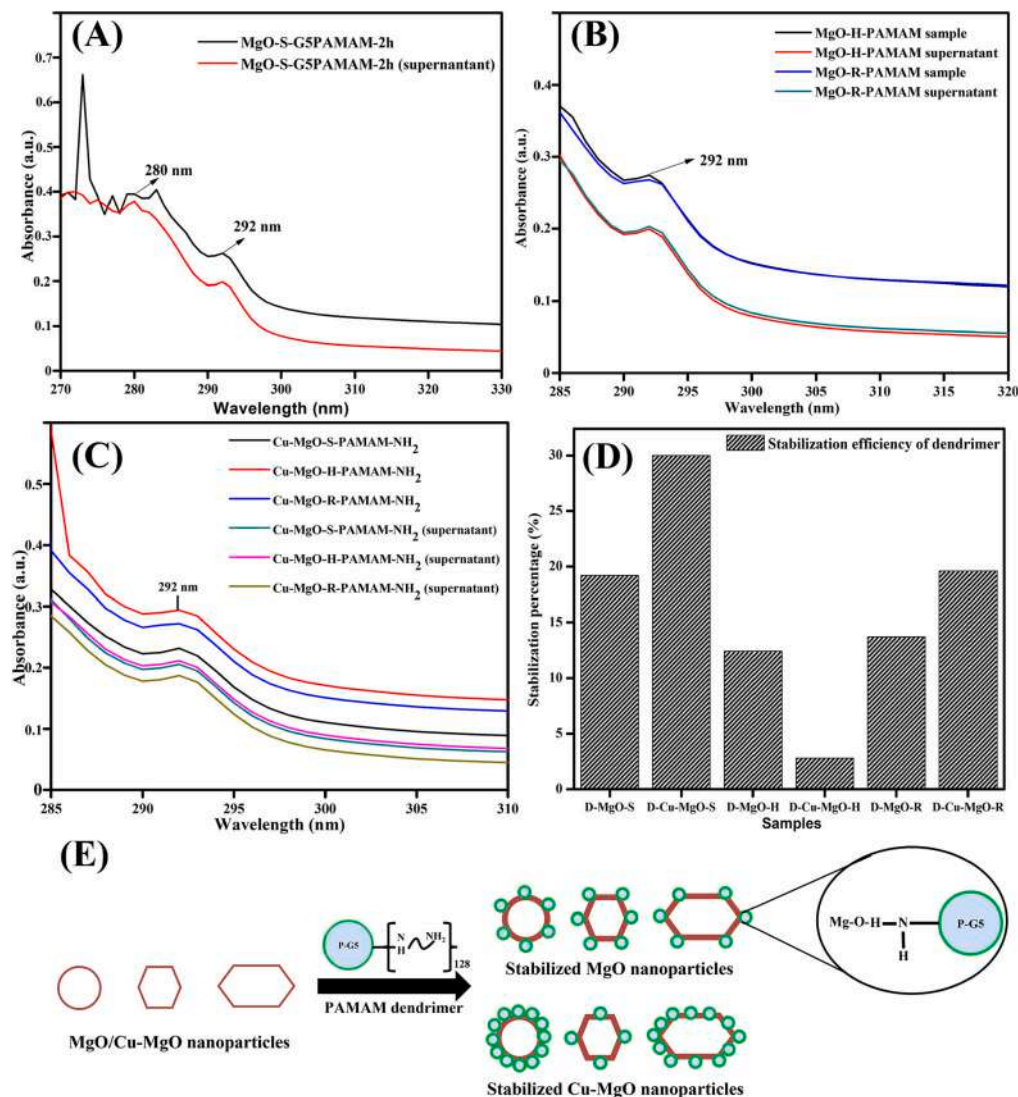


**Fig. 10.** UV–Visible spectra of G5-PAMAM dendrimer stabilized (A) MgO nanoparticles; (B) hexagonal and rod MgO nanoparticles; (C) Cu-doped MgO nanoparticles; (D) stabilization efficiency of G5-PAMAM dendrimer; (E) Proposed stabilization mechanism of different shapes of MgO nanoparticles with dendrimers. S – spherical, H – hexagon, R – Rod, G5-PAMAM – Fifth generation amine-terminated polyamidoamine dendrimer, D – Dendrimer, Cu – Copper ion as the dopant.

**Table 3**

Average size, PDI, and zeta potential of MgO, stabilized MgO, Cu-doped MgO, and stabilized Cu-doped MgO nanoparticles.

Sample	Size (d. nm)	Size (d. nm) supernatant	PDI	PDI supernatant	Zeta potential (mV)	Zeta potential (mV) supernatant
MgO-S	91.28		0.725		−2.91	
MgO-S-dendrimer	712.4 and 122.4	1400	0.395	1	12.2	5.69
MgO-H	78.82		0.430		−7	
MgO-H-dendrimer	458.7	1480	0.314	1	13	5.67
MgO-R	68.06		0.399		20.5	
MgO-R-dendrimer	955.4	1100	0.452	1	13.7	6.20
Cu-MgO-S	78.82		0.432		3.83	
Cu-MgO-S-dendrimer	615.1	1154	0.722	0.323	10.6	4.76
Cu-MgO-H	68.06		0.376		23.8	
Cu-MgO-H-dendrimer	966	1066	1	1	15.2	5.45
Cu-MgO-R	78.82		0.239		19.6	
Cu-MgO-R-dendrimer	881.4	6815	0.583	0.849	15.5	6.54

### 3.9. Functional group analysis of dendrimer stabilized MgO/Cu-doped MgO nanoparticles

The FTIR analysis (Fig. 11 and Table 4) using a KBr method, showed the presence of the primary amine group (NH<sub>2</sub>) (3295 cm<sup>−1</sup>) from the dendrimer and the = O vibrations (2127 cm<sup>−1</sup>), amides (−CO-NH−)

(1632 cm<sup>−1</sup>) and 664 cm<sup>−1</sup> (CH out of plane aromatic band) [110,111]. The variations in these peaks (MgO and Cu-doped MgO) show that certain portions of the MgO are exposed to dendrimer surface even after the stabilization, as indicated by maximum ~30 % stabilization efficiency. Thus, the comparative results of UV–Visible spectra, stabilization efficacy, DLS, and FTIR analysis has led to the selection of spherical

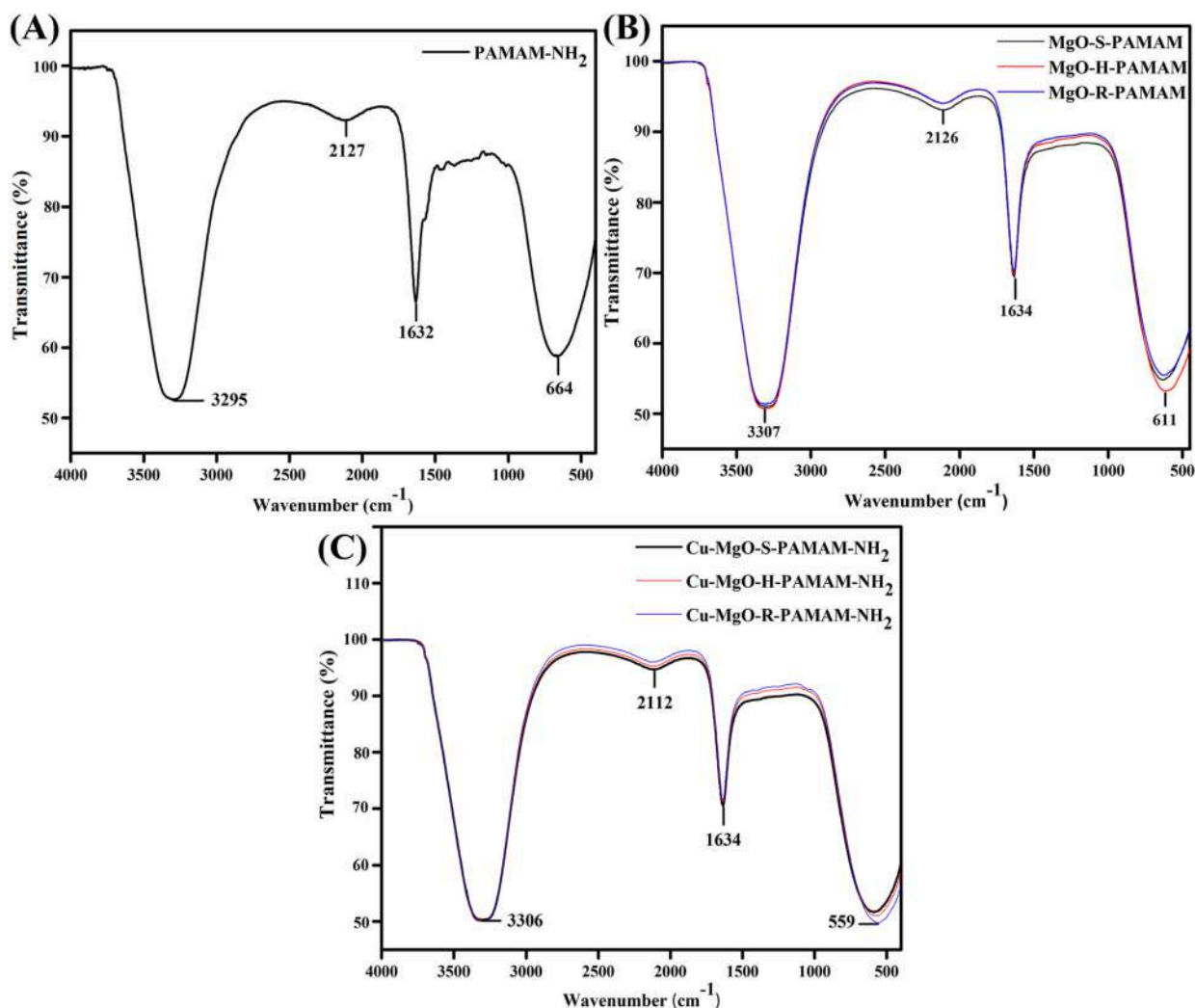


**Fig. 11.** FTIR spectra of (A) amine-terminated G5-PAMAM dendrimer; (B) different shapes of dendrimer stabilized MgO nanoparticles, and (C) different shapes of dendrimer stabilized Cu-doped MgO nanoparticles. S – Spherical, H – Hexagonal, R – Rod.

**Table 4**

FTIR spectral peaks of dendrimer stabilized MgO/Cu-doped MgO nanoparticle samples.

Sample	PAMAM	MgO-S-PAMAM	MgO-H-PAMAM	MgO-R-PAMAM
Peak (cm <sup>-1</sup> )	3295.00	3307.13	3307.03	3307.29
	2127.00	2126.65	2111.07	2114.94
	1632.08	1634.20	1634.35	1634.31
	664.61	631.44	611.49	619.96

Sample	PAMAM	Cu-MgO-S-PAMAM	Cu-MgO-H-PAMAM	Cu-MgO-R-PAMAM
Peak (cm <sup>-1</sup> )	3295.00	3306.71	3307.48	3307.31
	2127.00	2112.01	2122.99	2130.91
	1632.08	1634.29	1634.52	1634.50
	664.61	584.08	571.13	559.55

MgO nanoparticle samples stabilized using amine-functionalized G5-PAMAM dendrimer for further analysis.

### 3.10. Morphology analysis of dendrimer stabilized MgO/Cu-doped MgO nanoparticles

The SEM analysis, as in Figs. 12 (A) and (B) shows that the

nanoparticles were stabilized by dendrimers. The hollow spaces within the dendrimers (indicated by red arrow mark) represent the presence of MgO nanoparticles, stabilized by dendrimers. Since MgO nanoparticles are insulators or wide bandgap semiconductors and are smaller, it is impossible to view them via a 20-μm SEM scale. However, the stabilization of nanoparticles via dendrimers was clearly visible with larger size and agglomeration, which matches the DLS analysis.

### 3.11. Amylase inhibition activity of selected dendrimer stabilized MgO nanoparticle samples

Fig. 13(A) shows the alpha-amylase enzyme inhibition activity of free and PAMAM dendrimer stabilized MgO nanoparticles after 0 and 24 h. It can be noted that the 1 and 2 mg of nanoparticles yielded more maltose than the control samples (without MgO), which may be due to the catalytic effect of the enzyme under MgO influence. On the other hand, 3–4 mg of MgO nanoparticles promoted the inhibition of the alpha-amylase enzyme. In comparison, due to the agglomeration of nanoparticles, a 5 mg sample showed a higher enzymatic catalytic activity [112] (data in supplementary information section S.9). Hence, 3 mg of nanoparticles was selected for further enzyme inhibition analysis.

The results showed that non-stabilized MgO and metal-doped MgO possess a low alpha-amylase inhibition activity compared to the dendrimer stabilized samples at 0 h. Among the non-stabilized samples,



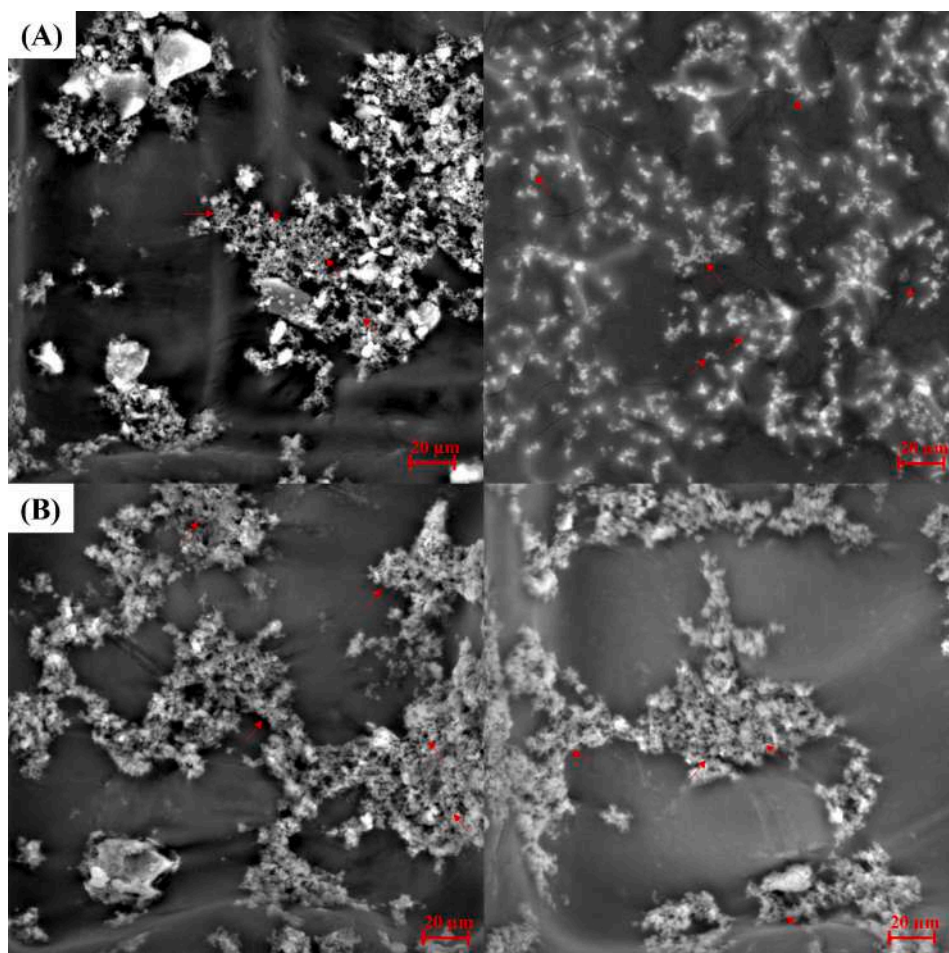


**Fig. 12.** Scanning electron micrograph of selected (A) G5 amine-terminated PAMAM dendrimer stabilized spherical MgO nanoparticles and (B) G5 amine-terminated PAMAM dendrimer stabilized spherical Cu-doped MgO nanoparticles.

MgO nanoparticles showed high enzyme inhibition activity due to reactive oxygen species (ROS) release. In contrast, Cu-doped MgO samples reduced the inhibition activity, where the copper ions acted as a catalyst to improve the amylase activity and convert starch to maltose [113,114]. It can be noted that the dendrimer stabilized samples showed enhanced enzyme inhibition activity compared to non-stabilized samples. This can be attributed to the amine group of the dendrimer (positive surface charge from DLS/ELS analysis), which may have been attached to the negatively charged site of the enzyme to release nanoparticles, eventually releasing ROS on the target site, inhibiting enzyme activity as proposed in Fig. 13 (B) [115–117]. The alpha-amylase inhibition activity of the non-stabilized and stabilized samples after 24 h shows that the inhibition activity of non-stabilized samples depends on the controlled release of ROS through stabilized NPs. The enzyme inhibition activity of the non-stabilized samples was improved after 24 h, whereas the dendrimer stabilized samples reduced the inhibition after 24 h. This shows that the release of ROS by the nanoparticles is controlled by the dendrimer-mediated stabilization and can be useful in prolonged inhibition of amylase enzyme [118,119].

Several previous studies have confirmed the amylase inhibition property of MgO nanoparticles [120,121]. These studies showed the immediate inhibition response of the nanoparticles by comparing them with commercial enzyme inhibitors named acarbose or metformin. It is worthy to note that the results of enzyme inhibition activity of the dendrimer stabilized MgO nanoparticles demonstrated in the present study is almost on par with the acarbose results and better than the MgO nanoparticle results from previous studies [121,122]. Further, D'Souza et al. [123] prepared zinc-doped MgO nanoparticles using the fruit

extract of *Vateria indica*. The study emphasized that the metal-doped nanoparticles possess enhanced enzyme inhibition efficacy compared to undoped MgO samples. The results in the present study are proximate to the previously reported for free MgO and Cu-doped nanoparticles at 0 h. The stabilization of nanoparticles with G5-amine-terminated PAMAM dendrimer is a major significance of this study, which eventually delays enzyme inhibition activity of nanoparticles at 0 h. Hence, it is evident from the results that the dendrimer enhances the amylase enzyme inhibition of MgO nanoparticles via controlled release and prolonged ROS effect for up to 24 h, when compared to free MgO nanoparticles. This could be beneficial in the long-term for controlled inhibition of amylase without rapidly increasing undigested starch in the intestine of diabetic patients. Although the effect of shape on the biological properties was not evaluated in this study, the presented results show that this aspect deserves to be considered in future studies.

#### 4. Conclusion

In this study, MgO and Cu-doped MgO nanoparticles were synthesized via sol-gel by optimization of calcination temperature and time approach. The nanoparticles' morphology and physicochemical properties were evaluated via a systematic characterization approach (e.g. SEM and TEM). Pure MgO and Cu-doped MgO nanoparticles were prepared in spherical, hexagonal, and rod/elongated rod shapes after the calcination process. Later, the fifth generation, amine-terminated PAMAM dendrimer suspended in an aqueous medium was selected for the stabilization of both MgO and Cu-doped MgO nanoparticles of distinct morphology. The efficiency of the dendrimer to stabilize

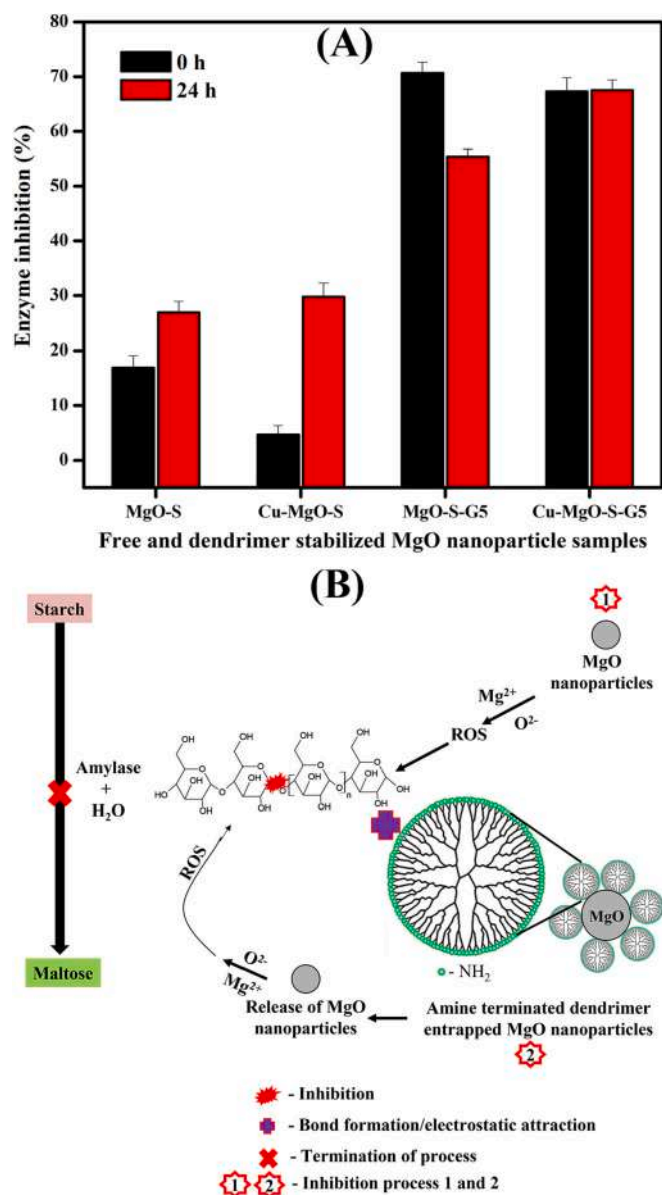


**Fig. 13.** (A) Alpha-amylase enzyme inhibition activity of free and PAMAM dendrimer stabilized MgO nanoparticles after 0 and 24 h; and (B) Proposed mechanism of alpha-amylase enzyme inhibition.

spherical copper-doped MgO nanoparticles (~30 %) is higher than in the other samples, which was confirmed by UV-Visible spectra, DLS, FTIR, and TEM analysis. The alpha-amylase inhibition assay emphasized that the dendrimer stabilization has prolonged the enzyme inhibition ability of MgO nanoparticles for up to 24 h.

This study will be a benchmark attempt to utilize dendrimer stabilized MgO nanoparticles for antidiabetic studies, especially for digestive enzyme inhibition. Further, this study can be extended to identify the potential of dendrimer formulation for inhibiting other enzymes with antidiabetic efficacy, compared with commercial enzyme inhibitors, other dendrimer generations with distinct functionalization units, and MgO nanoparticles doped with different metal ions.

#### Declaration of competing interest

The authors declare that they have no known competing financial interests or personal relationships that could have appeared to influence the work reported in this paper.

#### Data availability

Data will be made available on request.

#### Acknowledgment

This work was supported by FCT-Fundação para a Ciência e a Tecnologia through the CQM Base Fund - UIDB/00674/2020, by ARDITI-Agência Regional para o Desenvolvimento da Investigação Tecnológica e Inovação, through the project, M1420-01-0145-FEDER-000005 - Centro de Química da Madeira - CQM<sup>+</sup> (Madeira 14-20 Program). The authors acknowledge Laboratório Regional de Engenharia Civil (LREC), Madeira, Portugal, and Mr. Énio Fernandes (Assistant Technician) for their support to access TG-DTA and XRD equipment. The author (J. R.) acknowledges Programa de Cooperación Territorial INTERREG V-A MAC 2014-2020, Project Inv2Mac (MAC2/4.6d/229) for financial support, including a Post-Doc Grant for J.J. The author (R. C.) acknowledges ARDITI for the support under the scope of Project M1420-09-5369-FSE-000002, through a Post-Doc Grant.

#### Appendix A. Supplementary data

Supplementary data to this article can be found online at <https://doi.org/10.1016/j.bioadv.2023.213535>.

#### References

- [1] M.K. Danquah, J. Jeevanandam, Chapter 1 - the current state of diabetes treatment, in: M.K. Danquah, J. Jeevanandam (Eds.), *Emerging Nanomedicines for Diabetes Mellitus Therapeutics*, Elsevier, 2022, pp. 1–31.
- [2] K. Ogurtsova, L. Guariguata, N.C. Barengo, P.L.-D. Ruiz, J.W. Sacre, S. Karuranga, H. Sun, E.J. Boyko, D.J. Magliano, *Diabetes Res. Clin. Pract.* 183 (2022), 109118.
- [3] G.D. Ogle, S. James, D. Dabelea, C. Pihoker, J. Svensson, J. Maniam, E. L. Klatman, C.C. Patterson, *Diabetes Res. Clin. Pract.* 183 (2022), 109083.
- [4] G. Roglic, S.L. Norris, *Ann. Intern. Med.* 169 (2018) 394–397.
- [5] H. Mechchate, I. Es-Safi, A. Louba, A.S. Alqahtani, F.A. Nasr, O.M. Noman, M. Farooq, M.S. Alharbi, A. Alqahtani, A. Bari, *Molecules* 26 (2021) 293.
- [6] G. Grant, M. Duncan, R. Alonso, F. Marzo, Peas and lentils, in: B. Caballero (Ed.), *Encyclopedia of Food Sciences and Nutrition* (Second Edition), Academic Press, Oxford, 2003, pp. 4433–4440.
- [7] P.M. Sales, P.M. Souza, L.A. Simeoni, D. Silveira, *J. Pharm. Pharm. Sci.* 15 (2012) 141–183.
- [8] L. Gong, D. Feng, T. Wang, Y. Ren, Y. Liu, J. Wang, *Food Sci. Nutr.* 8 (2020) 6320–6337.
- [9] X. Nie, Z. Chen, L. Pang, L. Wang, H. Jiang, Y. Chen, Z. Zhang, C. Fu, B. Ren, J. Zhang, *Int. J. Nanomedicine* 15 (2020) 10215.
- [10] N. Sayed, A. Khurana, C. Godugu, *J. Drug Delivery Sci. Technol.* 53 (2019), 101201.
- [11] Y. Dong, B. Zhang, W. Sun, Y. Xing, Chapter 36 - intervention of prediabetes by flavonoids from *Oroxylum indicum*, in: R.R. Watson, V.R. Preedy (Eds.), *Bioactive Food as Dietary Interventions for Diabetes* (Second Edition), Academic Press, 2019, pp. 559–575.
- [12] M.K. Danquah, J. Jeevanandam, Chapter 5 - metal and metal oxide nanoparticles: synthesis, properties, and applications as nanomedicines for diabetes treatment, in: M.K. Danquah, J. Jeevanandam (Eds.), *Emerging Nanomedicines for Diabetes Mellitus Therapeutics*, Elsevier, 2022, pp. 111–142.
- [13] J. Iqbal, A. Andleeb, H. Ashraf, B. Meer, A. Mehmood, H. Jan, G. Zaman, M. Nadeem, S. Drouet, H. Fazal, *RSC Adv.* 12 (2022) 14069–14083.
- [14] B.A. Abbasi, J. Iqbal, T. Mahmood, A. Qyyum, S. Kanwal, *Appl. Organomet. Chem.* 33 (2019), e4947.
- [15] M.A. Ammulu, K. Vinay Viswanath, A.K. Giduturi, P.K. Vemuri, U. Mangamuri, S. Poda, *J. Genet. Eng. Biotechnol.* 19 (2021) 1–18.
- [16] W. Muhammad, M.A. Khan, M. Nazir, A. Siddiquah, S. Mushtaq, S.S. Hashmi, B. H. Abbasi, *Mater. Sci. Eng. C* 103 (2019), 109740.
- [17] M.D. Jayappa, C.K. Ramaiah, M.A.P. Kumar, D. Suresh, A. Prabhu, R.P. Devasya, S. Sheikh, *Appl. Nanosci.* 10 (2020) 3057–3074.
- [18] M. Shi, Y. Cen, G. Xu, F. Wei, X. Xu, X. Cheng, Y. Chai, M. Sohail, Q. Hu, *Anal. Chim. Acta* 1077 (2019) 225–231.
- [19] S. Dessai, M. Ayyanar, S. Amalraj, P. Khanal, S. Vijayakumar, N. Gurav, N. Rarokar, M. Kalaskar, S. Nadaf, S. Gurav, *Mater. Lett.* 311 (2022) 131639.
- [20] Y. He, S. Ingudam, S. Reed, A. Gehring, T.P. Strobaugh, P. Irwin, *J. Nanobiotechnol.* 14 (2016) 1–9.
- [21] M.A. Khan, F. Ali, S. Faisal, M. Rizwan, Z. Hussain, N. Zaman, Z. Afsheen, M. N. Uddin, N. Bibi, Saudi, *J. Biol. Sci.* 28 (2021) 5157–5167.
- [22] M.K. Patel, M. Zafaryab, M. Rizvi, V.V. Agrawal, Z.A. Ansari, B.D. Malhotra, S. G. Ansari, *J. Nanoeng. Nanomanuf.* 3 (2013) 162–166.
- [23] J. Jeevanandam, Y.S. Chan, M.K. Danquah, *New J. Chem.* 41 (2017) 2800–2814.
- [24] N.A. Abdulkhaleq, U.M. Nayef, A.K.H. Albarazanchi, *Optik* 212 (2020), 164793.

- [25] K.G. Rao, C.H. Ashok, K.V. Rao, C.S. Chakra, *Int. J. Sci. Res.* 3 (2014) 43–46.
- [26] H. Pereira, C.G. Moura, G. Miranda, F.S. Silva, *Opt. Laser Technol.* 142 (2021), 107181.
- [27] J. Jeevanandam, Y.S. Chan, M.K. Danquah, *ChemBioEng Rev.* 3 (2016) 55–67.
- [28] J. Jeevanandam, Y.S. Chan, M.K. Danquah, *Prot. Met. Phys. Chem. Surf.* 55 (2019) 288–301.
- [29] A.E. Danks, S.R. Hall, Z. Schnepp, *Mater. Horiz.* 3 (2016) 91–112.
- [30] M. Parashar, V.K. Shukla, R. Singh, *J. Mater. Sci. Mater. Electron.* 31 (2020) 3729–3749.
- [31] A. Kumar, N. Yadav, M. Bhatt, N.K. Mishra, P. Chaudhary, R. Singh, *Res. J. Chem. Sci.*, ISSN 2231 (2015) 606X.
- [32] M.V. Zdorovets, A.L. Kozlovskiy, *Vacuum* 168 (2019), 108838.
- [33] D. Khiev, Z.A. Mohamed, R. Vichare, R. Paulson, S. Bhatia, S. Mohapatra, G. P. Lobo, M. Valapala, N. Kerur, C.L. Passaglia, *Nanomaterials* 11 (2021) 173.
- [34] J. Panda, B.S. Satapathy, S. Majumder, R. Sarkar, B. Mukherjee, B. Tudu, *J. Magn. Magn. Mater.* 485 (2019) 165–173.
- [35] C.S. Camacho, M. Urgellés, H. Tomás, F. Lahoz, J. Rodrigues, *J. Mater. Chem. B* 8 (2020) 10314–10326.
- [36] I. Martins, H. Tomás, F. Lahoz, J. Rodrigues, *Biomacromolecules* 22 (2021) 2436–2450.
- [37] C. Camacho, H. Tomás, J. Rodrigues, *Molecules* 26 (2021).
- [38] S. Xiao, R. Castro, J. Rodrigues, X. Shi, H. Tomás, *J. Biomed. Nanotechnol.* 11 (2015) 1370–1384.
- [39] S. Mignani, J. Rodrigues, H. Tomas, R. Roy, X. Shi, J.-P. Majoral, *Adv. Drug Deliv. Rev.* 136–137 (2018) 73–81.
- [40] S. Mignani, J. Rodrigues, H. Tomas, A.-M. Caminade, R. Laurent, X. Shi, J.-P. Majoral, *Sci. China Mater.* 61 (2018) 1367–1386.
- [41] D.-M. Kim, S.-C. Jung, S. Ha, Y. Kim, Y. Park, J.H. Ryu, Y.-K. Han, K.T. Lee, *Chem. Mater.* 30 (2018) 3199–3203.
- [42] M. Ahmad, A.R.A. Usman, S.S. Lee, S.-C. Kim, J.-H. Joo, J.E. Yang, Y.S. Ok, *J. Ind. Eng. Chem.* 18 (2012) 198–204.
- [43] N.G. Schmahl, J. Barthel, G.F. Eikerling, *Z. Anorg. Allg. Chem.* 332 (1964) 230–237.
- [44] M. Paranthaman, K.A. David, T.B. Lindemer, *Mater. Res. Bull.* 32 (1997) 165–173.
- [45] B. Clavier, T. Baptiste, Z. Barbieriková, T. Hajdu, A. Guet, F. Boucher, V. Brezová, C. Roques, G. Corbel, *Mater. Sci. Eng. C* 123 (2021), 111997.
- [46] J. Jeevanandam, Y.S. Chan, M.K. Danquah, *ChemistrySelect* 2 (2017) 10393–10404.
- [47] X. Shi, K. Sun, L.P. Balogh, J.R. Baker, *Nanotechnology* 17 (2006) 4554.
- [48] X. Fuku, N. Matinise, M. Masikini, K. Kasinathan, M. Maaza, *Mater. Res. Bull.* 97 (2018) 457–465.
- [49] A. Seidell, *J. Am. Med. Assoc.* 91 (1928) 1131–1132.
- [50] S. Bhattacharjee, *J. Control. Release* 235 (2016) 337–351.
- [51] J. Jaison, S. Balakumar, Y. Chan, *IOP Conference Series: Materials Science and Engineering*, IOP Publishing, 2015, p. 012005.
- [52] S. Mianxince, B. Liang, Z. Tianliang, Z. Xiaoyong, *J. Rare Earths* 26 (2008) 693–699.
- [53] N. Aboulfotouh, Y. Elbasha, M. Ibrahim, M. Elok, *Ceram. Int.* 40 (2014) 10395–10399.
- [54] M. Sahu, P. Biswas, *Nanoscale Res. Lett.* 6 (2011) 1–14.
- [55] J. Jaison, S. Balakumar, Y.S. Chan, *IOP Publishing*, 2015, pp. 012005.
- [56] J. Jeevanandam, Y.S. Chan, M.K. Danquah, *ChemistrySelect* 2 (2017) 10393–10404.
- [57] M.A. Morsi, S.A. El-Khodary, A. Rajeh, *Phys. B* 539 (2018) 88–96.
- [58] T. Dippong, E.A. Leve, I.G. Deac, E. Neag, O. Cadar, *Nanomaterials* 10 (2020) 580.
- [59] R. Bhargava, P.K. Sharma, R.K. Dutta, S. Kumar, A.C. Pandey, N. Kumar, *Mater. Chem. Phys.* 120 (2010) 393–398.
- [60] M. Zahir, M.M. Rahman, K. Irshad, M.M. Rahman, *Nanomaterials* 9 (2019) 1773.
- [61] S. Sun, X. Zhang, Y. Sun, S. Yang, X. Song, Z. Yang, *Phys. Chem. Chem. Phys.* 15 (2013) 10904–10913.
- [62] A.M. Ismail, A.A. Menazea, H.A. Kabary, A.E. El-Sherbiny, A. Samy, *J. Mol. Struct.* 1196 (2019) 332–337.
- [63] M. Sajjad, I. Ullah, M.I. Khan, J. Khan, M.Y. Khan, M.T. Qureshi, *Results Phys.* 9 (2018) 1301–1309.
- [64] S.S. Chawhan, D.P. Barai, B.A. Bhanvase, *Therm. Sci. Eng. Prog.* 25 (2021), 100928.
- [65] V. Kusigerski, E. Illes, J. Blanus, S. Gyergyek, M. Boskovic, M. Perovic, V. Spasojevic, *J. Magn. Magn. Mater.* 475 (2019) 470–478.
- [66] C.W. Wong, Y.S. Chan, J. Jeevanandam, K. Pal, M. Bechelany, M. Abd Elkoudous, G.S. El-Sayyad, *J. Clust. Sci.* 31 (2020) 367–389.
- [67] J. Jeevanandam, Y.S. Chan, M.K. Danquah, *ChemistrySelect* 2 (2017) 10393–10404.
- [68] T. Tangcharoen, C. Kongmark, *J. Adv. Ceram.* 8 (2019) 352–366.
- [69] S. Chitra, P. Bargavi, M. Balasubramaniam, R.R. Chandran, S. Balakumar, *Mater. Sci. Eng. C* 109 (2020), 110598.
- [70] S. Meghana, P. Kabra, S. Chakraborty, N. Padmavathy, *RSC Adv.* 5 (2015) 12293–12299.
- [71] P.C. Dey, R. Das, *Indian J. Phys.* 92 (2018) 1099–1108.
- [72] W. Xie, J. Wang, L. Fu, Q. Tan, X. Tan, H. Yang, *Appl. Clay Sci.* 185 (2020), 105374.
- [73] S. Tomar, S. Gupta, S. Mukherjee, A. Singh, S. Kumar, R.K. Choubey, *Semiconductors* 54 (2020) 1450–1458.
- [74] S. Mustapha, M.M. Ndamitso, A.S. Abdulkareem, J.O. Tijani, D.T. Shuaib, A. K. Mohammed, A. Sumaila, *Adv. Nat. Sci. Nanosci. Nanotechnol.* 10 (2019), 045013.
- [75] N. Rani, S. Chahal, A.S. Chauhan, P. Kumar, R. Shukla, S.K. Singh, *Mater. Today: Proc.* 12 (2019) 543–548.
- [76] O.S. Oluwafemi, B.M.M. May, S. Parani, N. Tsolekile, *Mater. Sci. Eng. C* 106 (2020), 110181.
- [77] L. Martingana Pintarić, M. Somogi Škoc, V. Ljoljić Bilić, I. Pokrovac, I. Kosalec, I. Rezić, *Polymers* 12 (2020) 1210.
- [78] Z. Remes, H. Kozak, B. Rezek, E. Ukraintsev, O. Babchenko, A. Kromka, H. A. Girard, J.C. Arnault, P. Bergonzo, *Appl. Surf. Sci.* 270 (2013) 411–417.
- [79] S. Yousefi, B. Ghasemi, M. Tajalli, A. Asghari, *J. Alloys Compd.* 711 (2017) 521–529.
- [80] D. An, X. Ding, Z. Wang, Y. Liu, *Colloids Surf. A Physicochem. Eng. Asp.* 356 (2010) 28–31.
- [81] P. Tamilselvi, A. Yelilarasi, M. Hema, R. Anbarasan, *Nano Bulletin* 2 (2013), 130106.
- [82] G. Balakrishnan, R. Velavan, K.M. Batoo, E.H. Raslan, *Results Phys.* 16 (2020), 103013.
- [83] M. Shaheen, I.A. Bhatti, A. Ashar, M. Mohsin, J. Nisar, M.M. Almonee, M. Iqbal, *Z. Phys. Chem* 235 (2021) 1395–1412.
- [84] S. Muthukumar, R. Gopalakrishnan, *Opt. Mater.* 34 (2012) 1946–1953.
- [85] M. Ikram, T. Inayat, A. Haider, A. Ul-Hamid, J. Haider, W. Nabgan, A. Saeed, A. Shahbaz, S. Hayat, K. Ul-Ain, *Nanoscale Res. Lett.* 16 (2021) 1–11.
- [86] M. Manzoor, A. Rafiq, M. Ikram, M. Nafees, S. Ali, *Int. Nano Lett.* 8 (2018) 1–8.
- [87] C. Belkhaoui, N. Mzabi, H. Smaoui, P. Daniel, *Results Phys.* 12 (2019) 1686–1696.
- [88] D. Thamilvanan, J. Jeevanandam, Y.S. Hii, Y.S. Chan, *Can. J. Chem. Eng.* 99 (2021) 502–518.
- [89] P.J. Anderson, P.L. Morgan, *Trans. Faraday Soc.* 60 (1964) 930–937.
- [90] J. Amodeo, S. Merkel, C. Tromas, P. Carrez, S. Korte-Kerzel, P. Cordier, J. Chevalier, *Crystals* 8 (2018) 240.
- [91] K. Omri, S. Goudria, *J. Mater. Sci. Mater. Electron.* 32 (2021) 17021–17031.
- [92] A. Vanaja, M. Suresh, J. Jeevanandam, *Int. J. Nanosci. Nanotechnol.* 15 (2019) 277–286.
- [93] K.S. Ahmad, S.B. Jaffri, *Open Chem.* 16 (2018) 556–570.
- [94] A.R. Oganov, M.J. Gillan, G.D. Price, *J. Chem. Phys.* 118 (2003) 10174–10182.
- [95] M. Aslam, G. Gopakumar, T.L. Shoba, I.S. Mulla, K. Vijayamohan, S. K. Kulkarni, J. Urban, W. Vogel, *J. Colloid Interface Sci.* 255 (2002) 79–90.
- [96] V. Shanmugam, K.S. Jeyaperumal, *Appl. Surf. Sci.* 449 (2018) 617–630.
- [97] P. Nyamukamba, O. Okoh, H. Heroe, R. Taziwa, S. Zinya, *Synthetic methods for titanium dioxide nanoparticles: a review*, Chap. 8, Yang, D. (Ed.), (2018), *Titanium Dioxide - Material for a Sustainable Environment*. InTech. doi: <https://doi.org/10.5772/intechopen.70290>.
- [98] X. Guo, Q. Zhang, X. Ding, Q. Shen, C. Wu, L. Zhang, H. Yang, *J. Sol-Gel Sci. Technol.* 79 (2016) 328–358.
- [99] N. Sakai, T. Nakano, K. Yanaba, S. Imazeki, *J. Sol-Gel Sci. Technol.* 88 (2018) 379–385.
- [100] R.K. Singh, S. Kannan, *Mater. Sci. Eng. C* 45 (2014) 530–538.
- [101] A.T. Brant, D.A. Buchanan, J.W. McClory, P.A. Dowben, V.T. Adamiv, Y.V. Burak, L.E. Halliburton, *J. Lumin.* 139 (2013) 125–131.
- [102] H. Gupta, L.-S. Fan, *Ind. Eng. Chem. Res.* 41 (2002) 4035–4042.
- [103] C.-H. Lin, J.-H. Chao, C.-H. Liu, J.-C. Chang, F.-C. Wang, *Langmuir* 24 (2008) 9907–9915.
- [104] M.P. Nikolova, M.S. Chavali, *Biomimetics* 5 (2020) 27.
- [105] J.R. Morones, J.L. Elechiguerra, A. Camacho, K. Holt, J.B. Kouri, J.T. Ramirez, M. J. Yacamán, *Nanotechnology* 16 (2005) 2346.
- [106] H. Lee, R.G. Larson, *Molecules* 14 (2009) 423–438.
- [107] F. Avila-Salas, R.I. González, P.L. Ríos, I. Araya-Durán, M.B. Camarasa, *J. Chem. Inf. Model.* 60 (2020) 2966–2976.
- [108] Y. Shan, T. Luo, C. Peng, R. Sheng, A. Cao, X. Cao, M. Shen, R. Guo, H. Tomás, X. Shi, *Biomaterials* 33 (2012) 3025–3035.
- [109] Z. Xiong, C.S. Alves, J. Wang, A. Li, J. Liu, M. Shen, J. Rodrigues, H. Tomás, X. Shi, *Acta Biomater.* 99 (2019) 320–329.
- [110] Y. Zhang, X. Liu, L. Li, Z. Guo, Z. Xue, X. Lu, *Anal. Methods* 8 (2016) 2218–2225.
- [111] M. Mecozzi, M. Pietroletti, M. Scarpiniti, R. Acquistucci, M.E. Conti, *Environ. Monit. Assess.* 184 (2012) 6025–6036.
- [112] Y. Lin, J. Ren, X. Qu, *Acc. Chem. Res.* 47 (2014) 1097–1105.
- [113] L. Lo Leggio, T.J. Simmons, J.-C.N. Poulsen, K.E.H. Frandsen, G.R. Hemsworth, M. A. Stringer, P. Von Freiesleben, M. Tovborg, K.S. Johansen, L. De Maria, *Nat. Commun.* 6 (2015) 1–9.
- [114] S. Dakhmouch Djekrif, L. Bennamoun, F.Z.K. Labbani, A. Ait Kaki, T. Nouadri, A. Paus, Z. Meraihi, L. Gillmann, *Catalysts* 11 (2021) 1438.
- [115] Z. Han, H. Shaofeng, L. Zhang, F. Yunchang, G. Fengzhe, W. Dongyue, Z. Meijin, *Indian J. Biochem. Biophys.* 57 (2020) 411–431.
- [116] T.H. Nguyen, S.-L. Wang, A.D. Nguyen, M.D. Doan, T.N. Tran, C.T. Doan, V. B. Nguyen, *Mar. Drugs* 20 (2022) 283.
- [117] B.F. Shaw, G.F. Schneider, B. Bilgicer, G.K. Kaufman, J.M. Neveu, W.S. Lane, J. P. Whitelegge, G.M. Whitesides, *Protein Sci.* 17 (2008) 1446–1455.
- [118] A. Asthana, A.S. Chauhan, P.V. Diwan, N.K. Jain, *AAPS PharmSciTech* 6 (2005) E536–E542.
- [119] S. El Kazzouli, S. Mignani, M. Bousmina, J.-P. Majoral, *New J. Chem.* 36 (2012) 227–240.
- [120] M.A. Kainat, F. Khan, S. Ali, M. Faisal, Z. Rizwan, N. Hussain, Z. Zaman, M. N. Afsheen, N. Uddin, Bibi, Saudi, *J. Biol. Sci.* 28 (2021) 5157–5167.

- [121] M.A. Ammulu, K. Vinay Viswanath, A.K. Giduturi, P.K. Vemuri, U. Mangamuri, S. Poda, J. Genet. Eng. Biotechnol. 19 (2021) 21.
- [122] A.A.-A. Ahlam, N.A.E.-R. Soheir, Food Nutr. Sci. 12 (2021) 308.
- [123] J.N. D'Souza, G.K. Nagaraja, K. Meghana Navada, S. Kouser, D.J. Manasa, Ceram. Int. 47 (2021) 29620–29630.